LIFE PREDICTION ANALYSIS OF A SUBSCALE ROCKET ENGINE COMBUSTOR USING A

FLUID-THERMAL-STRUCTURAL MODEL

Except where reference is made to the work of others, the work described in this thesis is my own or was done in collaboration with my advisory committee. This thesis does not include proprietary or classified information.

_____

Rohit Sarwade

Certificate of Approval:

_____   _____

Robert S. Gross   Winfred A. Foster Jr., Chair
Associate Professor   Professor
Aerospace Engineering Department   Aerospace Engineering Department

_____   _____

Hareesh V. Tippur   Stephen L. McFarland
Professor   Acting Dean
Mechanical Engineering Department   Graduate School

Life Prediction Analysis of a Subscale Rocket Engine Combustor using a

Fluid-Thermal-Structural Model

Rohit Sarwade

A Thesis

Submitted to

the Graduate Faculty of

Auburn University

in Partial Fulfillment of the

Requirements for the

Degree of

Master of Science

Auburn, Alabama

May 11, 2006

LIFE PREDICTION ANALYSIS OF A SUBSCALE ROCKET ENGINE COMBUSTOR USING A

FLUID-THERMAL-STRUCTURAL MODEL

Rohit Sarwade

_____

Signature of Author

_____

Date of Graduation

Rohit Sarwade, son of Vidyadhar and Vidya Sarwade, was born on August 21, 1982, in Pune, India. He graduated from M.E.S Garware College, Pune in 1999. He attended Vishwakarma Institute of Technology (V.I.T), Pune University, Pune and graduated first class with distinction with a Bachelor of Science degree in Mechanical Engineering in August, 2003. He joined the graduate program in Aerospace Engineering at Auburn University in August 2003.

Thesis Abstract

Life Prediction Analysis of a Subscale Rocket Engine Combustor using a

Fluid-Thermal-Structural Model

Rohit Sarwade

Master of Science, May 11, 2006
(B.S., Pune University, 2003)

92 Typed Pages

Directed by Winfred A. Foster, Jr.

The focus of this thesis was on performing a non-linear transient fluid-thermal-structural analysis of the cooling jacket for a scale model rocket engine thrust chamber. The model was for a water cooled annular plug nozzle thruster. The objective of this work was to predict the number of firing cycles the chamber could undergo without failure. The analysis consisted of multiple temperature and pressure firing cycles representing startup, shutdown and steady state operation of the engine. Two separate numerical codes combining fluid, thermal and structural analyses were used to obtain the solution. Non-linear strains were observed after 20 firing cycles and failure was predicted to occur after 255 cycles.

Style manual or journal used Journal of Approximation Theory (together with the style known as "aums"). Bibliograpy follows van Leunen's *A Handbook for Scholars.*

Computer software used The document preparation package T_EX (specifically L^AT_EX) together with the departmental style-file `aums.sty`.

Table of Contents

CHAPTER 1

INTRODUCTION

This project was performed in conjunction with the Rocket Engine Advancement Program (REAP)2 Program. NASA formed the REAP2 Program as a collaborative university research effort organized under the Constellation University Institutes Project (CUIP) with a mission focused on research and education in advanced propulsion for space exploration. In the development of its 2nd generation launch vehicle propulsion systems, NASA has been putting heavy emphasis on reusable rocket engines. The need to achieve long life and reusability in liquid rocket engines depends in large part upon design of the thrust chamber cooling system.

The first high performance rocket engine designed for multiple uses was NASA's Space Shuttle Main Engine (SSME). However, structural failures such as cracks in the main combustion chamber liner walls have been one of the main factors in reducing the usable life of the engines. These cracks, due to large thermal and pressure induced plastic strain cause the wall between the coolant and gas side to deform and progressively thin with each thermal cycle eventually leading to failure[3]. This report presents an analysis methodology which has the potential to improve the efficiency and accuracy of the design process. This process would allow a more accurate determination of the variables influencing the design and would reduce the overall time to complete the analysis.

A subscale prototype combustor was designed, built and tested at the Purdue University School of Aeronautics and Astronautics. The experimental data obtained from these tests is used extensively in this work. The emphasis of the work on the REAP2

program at Auburn University Aerospace Engineering Department was to develop a coupled fluid-thermal-structural analysis by combining commercially available software packages. This had the advantage of using proven numerical techniques, each of which were well known to a large number of users.

The project started with a baseline steady state two-dimensional finite element analysis to make initial comparisons with the experimental data. The two-dimensional steady-state model was modified to study start-up and shut-down transient thermal loads. Later non-linear material effects were incorporated into the transient model. The next stage was the development of a steady state three-dimensional model, which was followed by the incorporation of non-linear and transient effects to perform an uncoupled thermal-structural analysis. The current task and the focus of this thesis was to incorporate a computational fluid dynamics model into the analysis and perform a fluid-thermal-structural analysis.

The two-dimensional model turned out to be inadequate. The model gave acceptable thermal results, but the strain results were inaccurate. To overcome these inaccuracies a three-dimensional model was developed. The three-dimensional model led to an increase in computational resources required, but the results obtained were closer to the experimental results obtained at Purdue. The use of a simplified model to evaluate the thermal boundary conditions on the cooling jacket was one of the reasons for the inaccuracies in the results. The emphasis of this research was to incorporate a CFD code to model the combustion chamber gas and coolant fluid behavior giving a more accurate and complete solution and use minimum time and computer resources. The first attempt was to use a single solver which could perform the fluid-thermal-structural coupled analysis. MSC/Dytran® and MSC/Marc® were tried, but neither had the capability to do

the fully coupled solution at the present time. Thus it was a decided that two separate codes, fluid-thermal and thermo-structural, would be used. The two codes chosen were FLUENT® for the fluid-thermal solution and MSC/Marc® for the thermo-structural analysis.

A review of the literature on life estimation of rocket engine thrust chambers is presented in chapter 2. The modeling and analysis performed in this project are explained in detail in chapter 3. Chapter 4 discusses the results and chapter 5 presents the conclusions obtained from this analysis.

CHAPTER 2

BACKGROUND

Materials used in rocket engine combustion chambers undergo severe temperature and pressure loading. Temperatures and pressures in the space shuttle main engines can reach as high as 6000 F and 3000 psi. Cooling the thrust chamber is a major problem which must be solved. Some form of liquid cooling is one of the most common ways to cool the thrust chamber. It is necessary to use materials with high thermal conductivity to ensure that maximum heat transfer to the coolant is obtained so that the loss in structural strength is minimized. High strength and creep resistance are also necessary properties for chamber materials. The yield strength of most metals decreases as the temperature increases and the cyclic loading causes strain hardening of the material in the plastic region.

It has been observed that for a shorter cyclic loading period fatigue is the dominant failure mechanism while for longer loading times creep is the more dominant factor. Other failures that could occur in the chamber are buckling due to high axial pressures at higher temperatures where the materials undergo loss in strength, corrosion and abrasion due to repeated firings in the combustion chamber[1]. Interaction of fatigue and creep has also been observed to occur causing progressive deformation and thinning of the coolant wall and is also called plastic ratcheting or thermal ratcheting[3].

NASA in the 1970's started a number of life prediction studies on thrust chambers subjected to cyclic loading. The focus was on the mechanical properties of metals and alloys such as OFHC copper and NARloy-Z. Armstrong and Brogren[10] (1975)
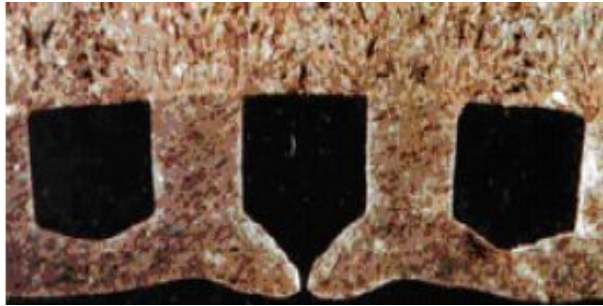
Figure 2.1: Dog-house effect or thinning and bulging of coolant passage wall towards chamber centerline (source: Ellis[12] (1999).

continued the work started by Esposito and Zabora[11] (1975) on material analysis by performing numerical thermo-mechanical studies of fatigue behavior on such materials. Quentmeyer[3] (1977) performed experimental studies on fatigue life of thrust chambers during which he observed that failure occurred by thinning of the cooling passage wall, bulging of the wall towards the thrust chamber centerline and severely deformed cooling channel cross-section geometry. Because of its final shape this kind of failure was called the "'dog-house"' effect. Jankovsky[4] (1995) et al. validated analytically and experimentally effects of cyclic dependent creep as a possible mode of failure. Figure 2.1 shows a magnified view of the failed passage wall as observed by Ellis[12] during experiments on a copper alloy chamber liner.

Armstrong and Brogren[13] (1976) used a two-dimensional finite element analysis code, BOPACE 2-D, capable of solving for elastic, plastic, creep and thermal strains. Their results concluded that the life of the chamber depends on the operating temperature and the temperature dependency of the material properties. They continued the investigation with a three-dimensional finite element analysis using BOPACE 3-D to perform the structural analysis and Boeing Engineering Thermal Analyzer (BETA) to compute the thermal effects. After comparing the two-dimensional and three-dimensional

analyses they concluded that the two-dimensional analysis gave accurate temperatures but for correct strain output a three-dimensional analysis was necessary.

Quentmeyer[3] (1977) also found a relation between the possible number of cycles to failure, the temperature at the thrust chamber inner radius and the temperature difference across the chamber wall and coolant wall. Further studies were performed by Kasper[5](1984) using fatigue and creep as the failure basis and by Porowski[6] et al. (1985) by simplifying the coolant section geometry into a rectangular beam. Dai and Ray[7] (1995) improved on this by using a time dependent visco-plastic model thought to be important for the considered materials.

Armstrong[14] (1979) studied the dog-house effect observed in Quentmeyer's[3] (1977) experimental results and suggested that coolant section geometry modifications might lead to longer cyclic life possibilities. The bulging and thinning of the OFHC copper coolant walls was also observed during experiments by Hannun and Price [15] (1981). They constructed models based on the bulging and thinning results from the computer code Systems Improved Numerical Differencing Analyzer (SINDA) and observed that it had very little effect on temperatures at thrust chamber inner radius. This was because the increased temperature due to bulging was compensated by the decrease in temperature due to the thinning of the coolant walls. They also concluded that surface roughening during cyclic loading caused a considerable increase in the heat transfer coefficient at the gas chamber wall. This parameter was taken into consideration in their analysis and an increase in temperatures across the coolant channel wall was observed.

Robinson and Arnold [16] (1990) also investigated the creep, thinning and bulging effects of the chamber, done initially by Quentmeyer[3] (1977). This and further experiments by Arya and Arnold expanded on Robinson's[17] (1982) earlier inelastic constitutive model. Robinson and Arnold focused on using an experimental viscoplastic model (combined plasticity and creep phenomenon) while Arya and Arnold[18] (1992) also used the viscoplastic model to perform a finite element analysis on a cylindrical thrust chamber liner composed of NARloy-Z. Arya and Arnold did not observe the thinning and bulging or dog-house effect observed by Quentmeyer[3] (1977) and concluded that the pressure difference across the coolant wall and inelastic behavior contributed to the effect. The two-dimensional finite element model used by them is shown in figure 2.2. The results for deformation on both pressure and thermal loading and thermal loading only are observed by them are as seen in figures 2.3 and 2.4.

Zhu[9] et al. (2004) demonstrated oxidation and creep enhanced fatigue cracking in their experiments on metal surfaces. They applied cyclic laser loads to study fatigue characteristics of combustor materials. They also observed that material surface oxidation and creep enhanced fatigue is an important mechanism for the surface crack initiation and propagation. The cyclic temperature loading applied by Zhu is as shown in figure 2.5. The effects of thermal ratcheting observed in their analysis is shown in figure 2.6.

Freed and Verrilli[19] (1988) worked on a viscoplastic theory applied to copper in which they derived a phenomenologically based viscoplastic model for copper. Their objective was to create a relatively simple viscoplastic model with the capability of providing accurate input to life assessing schemes. Their model did a good job in predicting
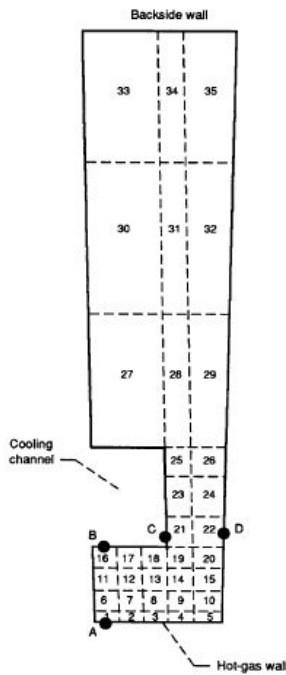
Figure 2.2: Two-dimensional finite element model for cylindrical thrust chamber (source: Arya and Arnold[18] (1992).

thermomechanical results like strain rates at the hot end of the cycle but overpredicted the cold end of the cycle.

Jankovsky and Kazaroff[20] (1990) studied the difference between a tubular shape and a milled rectangular channel for coolant flow and concluded that tubes are a possible replacement for the existing milled channel configuration since it offers increased surface area for additional enthalpy extraction, it has ideal pressure vessel characteristics and the shape of the tube is believed to allow free expansion, thus accommodating the strain resulting from thermal expansion. They performed a two-dimensional finite element analysis to compare their results with experimental results and provide a life comparison for the two shapes.

1st Cycle   12th Cycle

Figure 2.3: Deformed shapes (magnified) on short cyclic pressure and thermal loading, a)1st cycle b) 12th cycle (source: Arya and Arnold[18] (1992).

Sung[1] et al. (2003) performed an experimental analysis of a subscale rocket engine combustor as part of the Rocket Engine Advancement Program II (REAP II). They used a water cooled, 200 psia combustor that used decomposed hydrogen peroxide as the oxidizer and JP-8 as the fuel. They predicted the combustor life cycle for low cycle thermal stress, transient effects, and creep rupture damage on conventional and visco-plastic models. Sung observed considerable radial inward deformation and silver spots due to high local temperatures at the throat section and also surface roughening similar to the that noticed by Quentmeyer[3] (1977). The chamber liner before and after deformation are as shown in figure 2.7 and figure 2.8.

Sung[1] et al. (2003) used various life estimation methods to support their experimental results. Using the Poroski method they obtained a life prediction of 51 cycles,
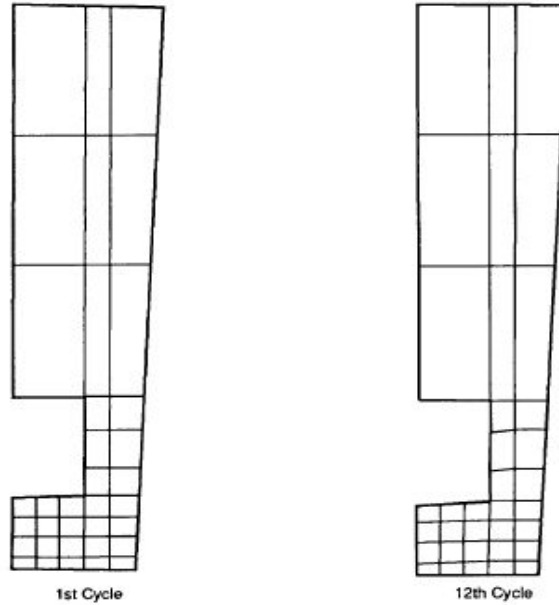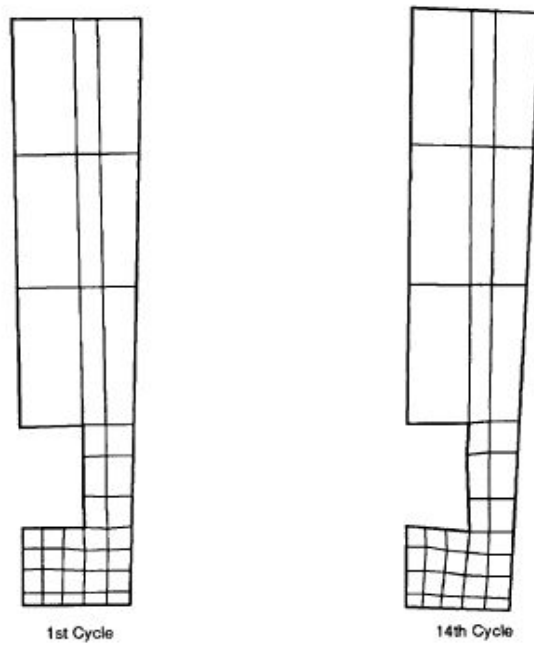
Figure 2.4: Deformed shapes (magnified) after short cyclic thermal loading only a)1st cycle b) 14th cycle (source: Arya and Arnold[18] (1992).
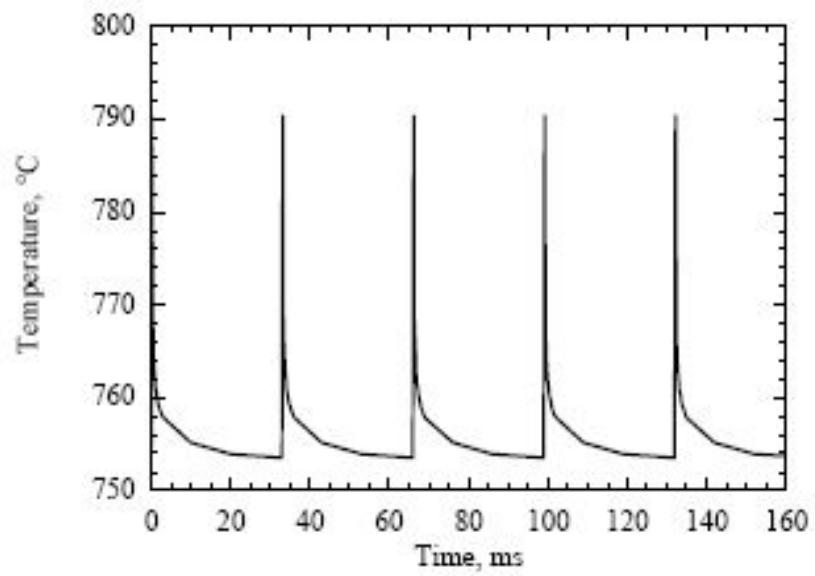
Figure 2.5: Temperature Loading (source: Zhu [9] (2004).
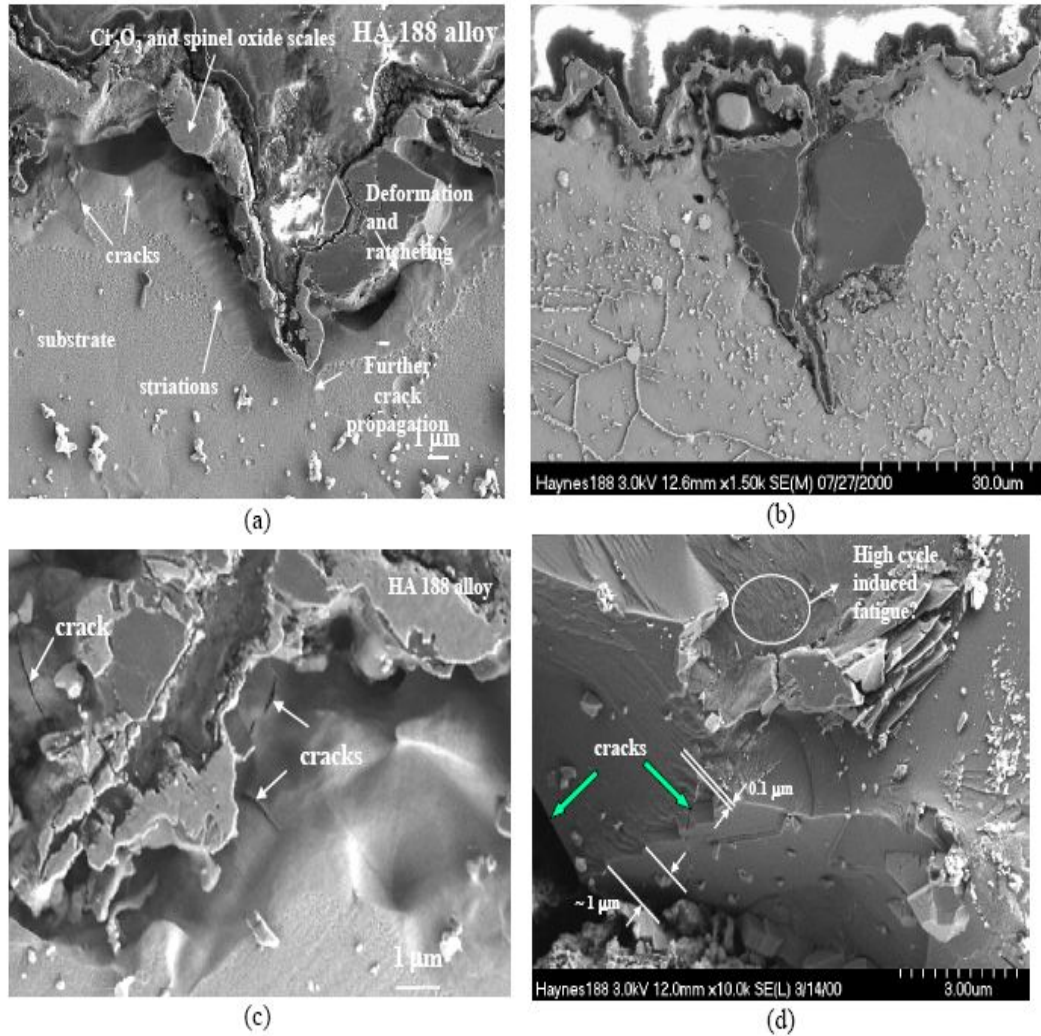
Figure 2.6: Thermal Ratcheting, (a) and (b) Cross-sections of the specimen showing a surface crack penetrating into the alloy and associated oxide scale-alloy substrate fatigue striation and crack initiation. (c) and (d) Microcracks and fatigue striations initiated in the alloy at the alloy/oxide interface under the surface cyclic thermal stresses. (source: Zhu [9] (2004).

Figure 2.7: Undeformed OFHC Copper Chamber Liner (source: Anderson [21] (2003).
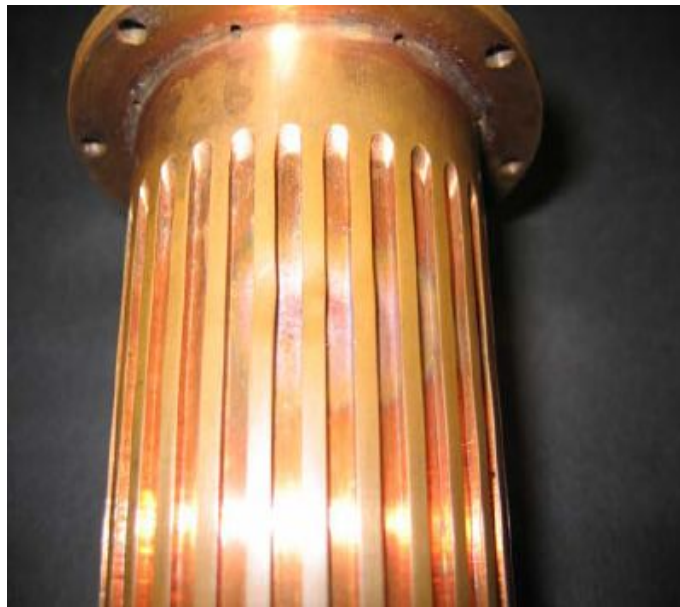
Figure 2.8: Deformed OFHC Copper Chamber Liner observed at the throat section by the silver spots (source: Anderson [21] (2003).

115 using the Effective stress-strain method, 115 cycles using a ANSYS two-dimensional finite element analysis and 320 cycles using a ABAQUS two-dimensional finite element analysis.

Sung[1] et al. (2003) performed an analytical analysis based on Dai and Ray's[7] sandwich beam model and viscoplacticity to represent progressive bulging and thinning phenomena in the coolant channel of their experimental model. Their experimental model is the same model that was used in the analysis performed for this project. A life of 260 cycles before failure occurs was predicted using this methodology.

CHAPTER 3

THRUST CHAMBER MODEL

3.1 Cooling Jacket Modeling Approach

Modeling the thrust chamber cooling jacket for the thermo-structural stress analysis was done in two stages. The first stage was a fluid-thermal analysis in which both, the solid and fluid zones had to be modeled. The second stage was a thermo-structural analysis in which only the solid zone was modeled. Two different solvers were used for the two related analysis and data from the first analysis were transferred to the second analysis to complete the problem definition.

A schematic drawing of the complete engine assembly is shown in figure 3.1. The geometry of the thrust chamber model is shown in figures 3.2 to 3.8. Figure 3.2 and 3.3 show views at the inlet and outlet of the model including of the center body. Isometric views on the inlet and outlet faces are shown in figures 3.4 and 3.5 respectively. The coolant channels, liner and close-out make up the cooling jacket and are shown in figure 3.6. The experimental model of the thrust chamber cooling jacket is shown in figure 2.7. Figure 3.7 shows the center body model while the center body for the experimental analysis is shown in figure 3.8.

The thrust chamber modeled had an annular plug nozzle in which the center body defines the nozzle shape and the coolant walls and passageways remain cylindrical in shape. The model consisted of a copper center body and copper and steel cylindrical walls with coolant channels between them. There were 30 coolant channels in the cooling jacket. The center body had a radius of 0.4" at the inlet, 0.4" at 1.825" length, 0.842"

14

To Ox Main Valve
500 psi 90% H202
½" AN Fitting

P_Oxcatout
¼" AN Fitting
200 psi

T_Catout
1/16" Swagelok Fitting
1200 degrees F

Engine Mount Bolts to
(4) Unitstrut L-brackets
On Test Stand w/(4) ½" bolts

To Fuel Main Valve
250 psi RP-1
1/2" AN Fitting

T_Precombustor
Welded
260 degrees F

P_Chamber1
¼" AN Fitting
200 psi

P_Chamber2
¼" AN Fitting
200 psi

P_CBin
¼" AN Fitting
100 psi

To Water Main Valve
200 psi H20
1/2" AN Fitting

T_Jackin
1/16" Swagelok Fitting
71 degrees F

P_Jackin
¼" AN Fitting
100 psi

T_Jackout1
1/16" Swagelok Fitting
150 degrees F

P_Jackout
¼" AN Fitting
80-100 psi

T_Jackout2
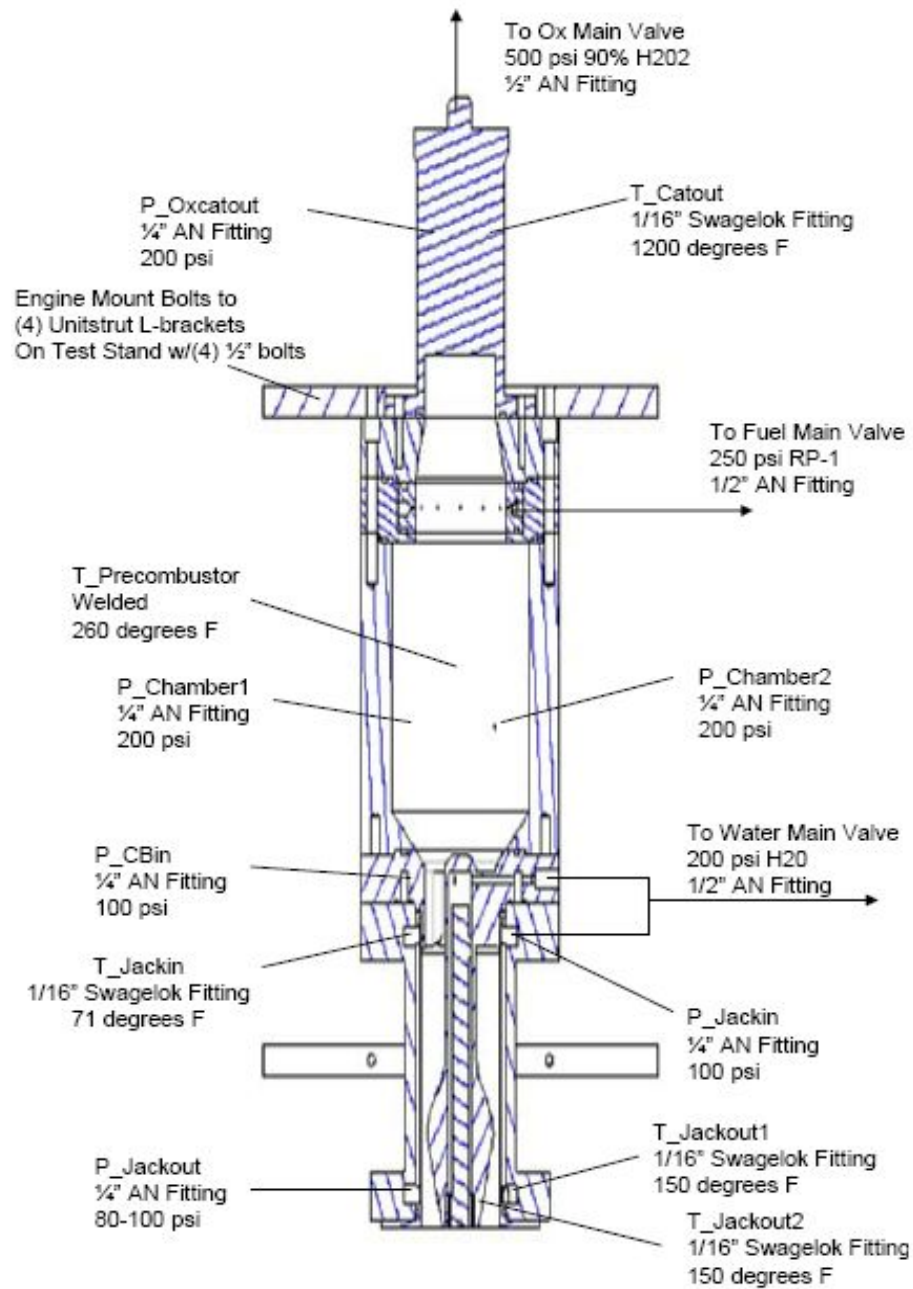1/16" Swagelok Fitting
150 degrees F

Figure 3.1: Sectional Details of the Experimental Model (source: Anderson[21] et al. (2003)).
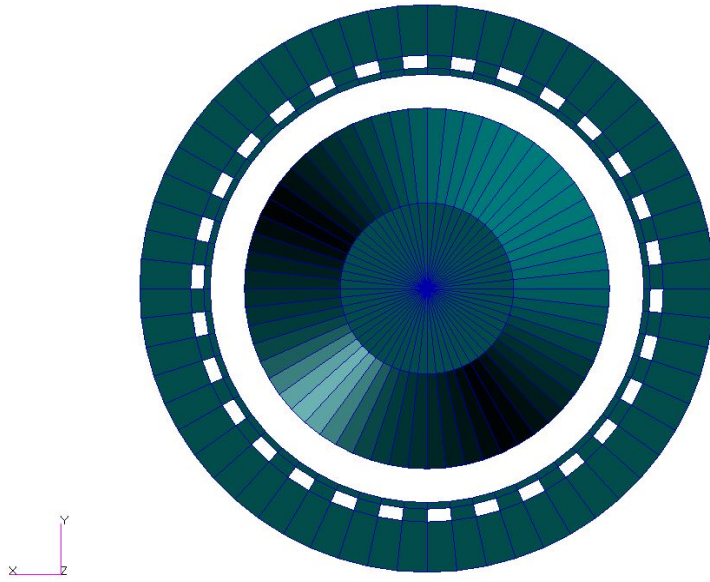
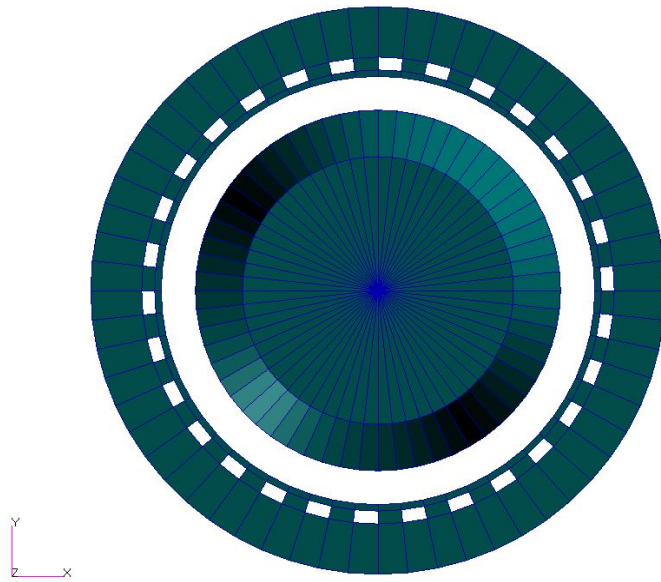Figure 3.2: View from Inlet of Chamber with the Center Body.

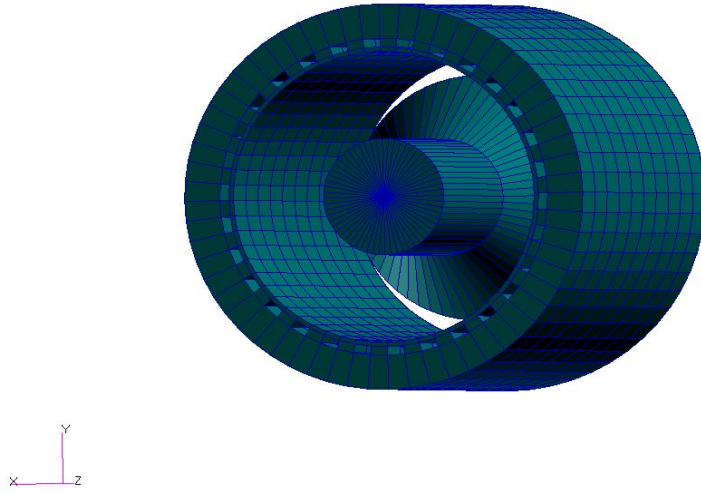Figure 3.3: View from Outlet of Chamber with the Center Body.
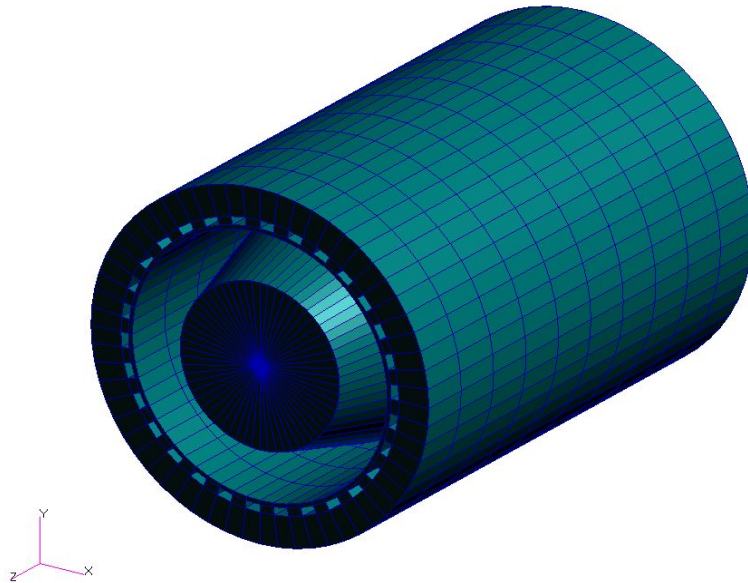
Figure 3.4: Isometric View on Inlet Side.

Figure 3.5: Isometric View on Exit Side.
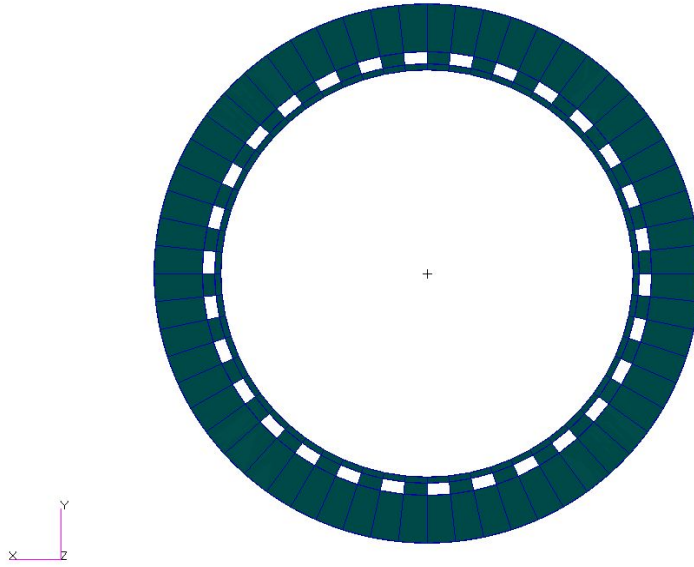
Figure 3.6: View of Chamber without the Center Body as used for structural analysis.
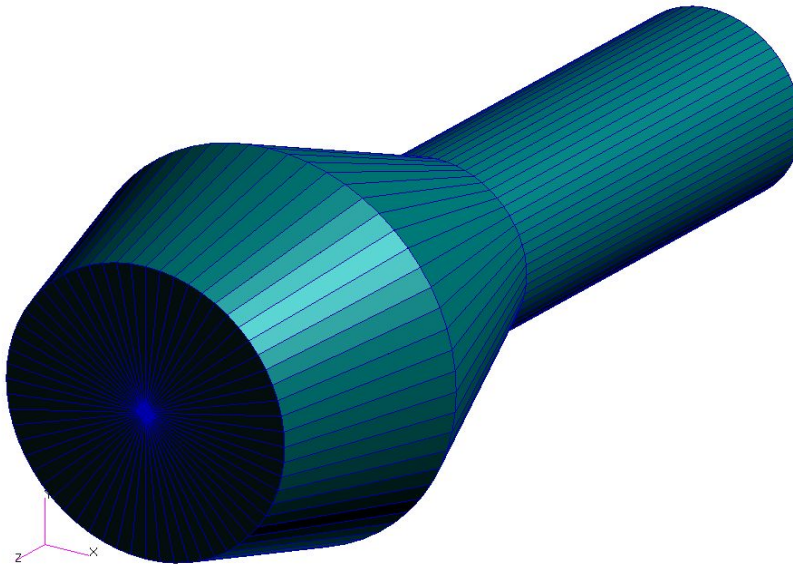

Figure 3.7: Center Body Model

18

Figure 3.8: Center Body used in the Experimental Analysis (source: Anderson[21] et al. (2003).

at the throat section 2.949" from the inlet and 0.46" at the exit, 4" from the inlet. The cooling passages extended to a distance of 3.775" from the inlet to the end of the combustion chamber and this is the portion that was modeled. The inner radius of the copper cylinder was 1", the outer radius was 1.03", the inner radius of the steel closeout was 1.09" and the outer was 1.375". The coolant side walls were also made of copper. A cyclicly symmetric model was constructed using a 12° section of the complete model and consisted of one of the thirty cooling channels and the surrounding copper and steel walls. The geometry of the model is as shown in figures 3.9 to 3.11. Figure 3.9 shows a magnified view of the annular region of the chamber of which a section was modeled. An Isometric view of the sectional model is shown in figure 3.10. Figure 3.11 shows the cross-sectional view of the section.
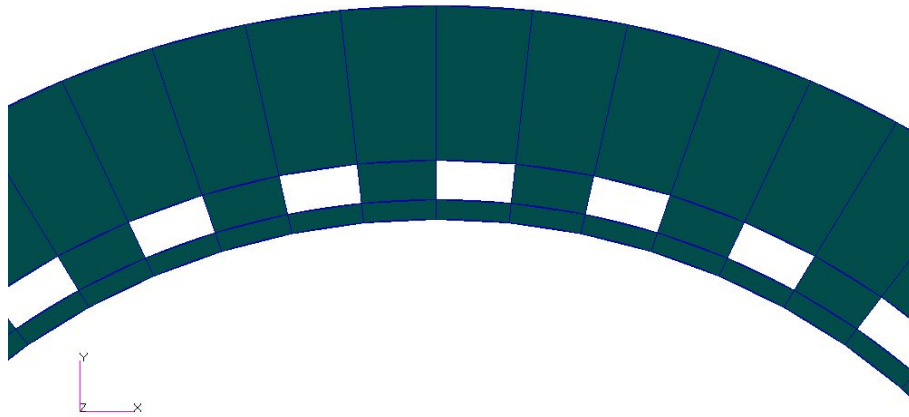
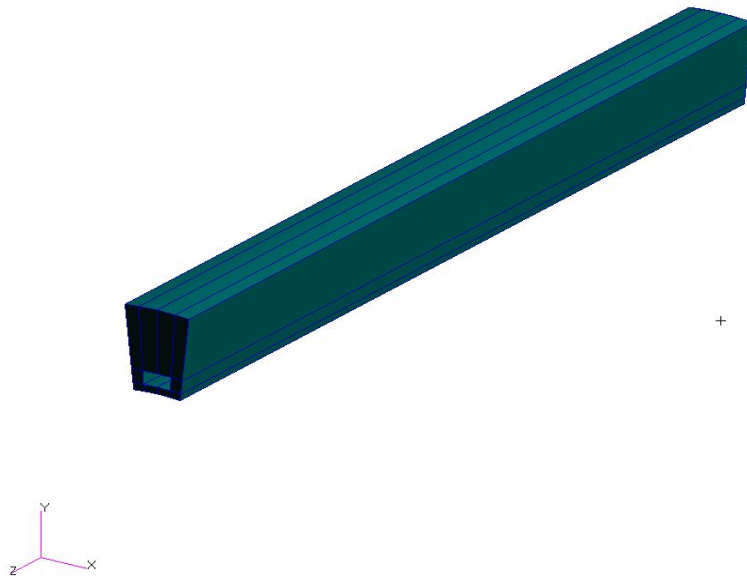Figure 3.9: Magnified region of interest for using the symmetric nature of the model.

Figure 3.10: Isometric view of the sectional symmetric model.

20
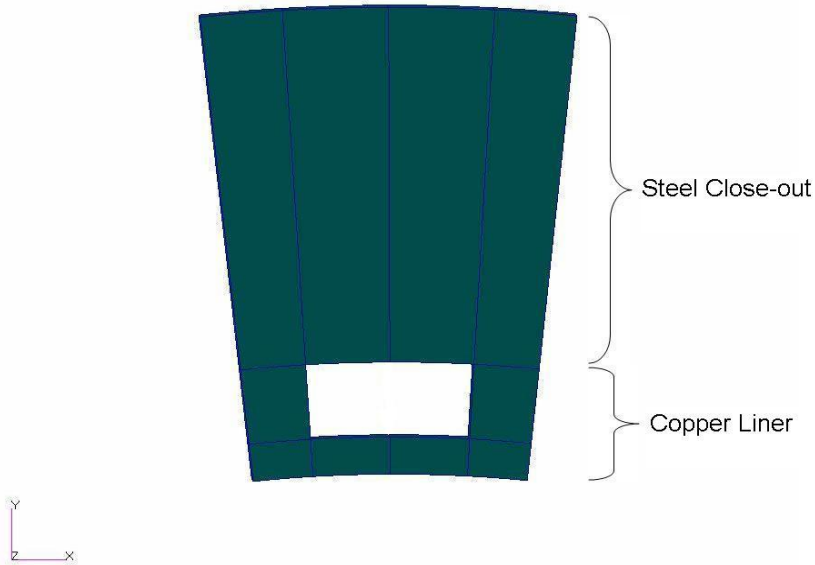
Figure 3.11: Sectional view of the symmetric model.

3.2 Fluid-Thermal Analysis Model

The geometry of the fluid-thermal model was created using Gambit® as the pre-processor. This included modeling both, the fluid zone and the solid zone. An initial uniform interval spacing mesh was also created in Gambit® for both zones. A non-uniform mesh concentrated at the fluid wall boundaries was created by refining the mesh at the boundaries in Fluent®. This was done using the thermal gradients in the boundary layer between the gas and copper wall, and of the coolant water with the copper and steel walls as the refining criteria. Because of its geometry the gas region of the model consisted of an unstructured mesh consisting of tetrahedral elements, while a structured mesh for the solid and water regions was possible due to their simple rectangular geometry. The mesh and related boundary conditions were then input to

Figure 3.12: Meshed Fluid-Thermal Model

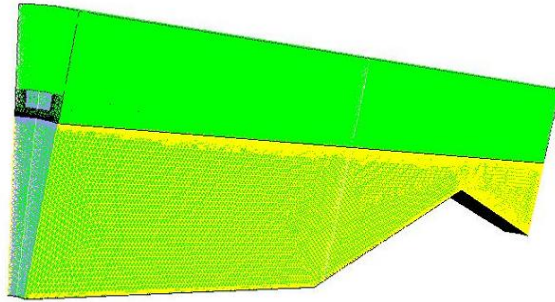Fluent®. The mesh was checked and corrected for any skewed elements and also resized to the actual model units. The fluid-thermal model consisted of 2,768,338 cells and 688,140 node points. Symmetry options on the fluid and solid side walls of the 12° section about the Z axis were used while creating the geometry and mesh in Gambit®. The geometry and mesh input for the fluid-thermal model is as shown in figures 3.12 and 3.13. Figure 3.12 shows the isometric view of the meshed model from the inlet side and figure 3.13 shows the sectional view on the outlet side. In figure 3.12 the fluid zones are represented by the yellowish green region and the solid copper and steel regions in green. The gray faces represent the gas and water inlets, the black face represents the copper region at the inlet side and green face, the steel region. The reddish green faces in figure 3.13 represent the gas and water outlet boundaries.
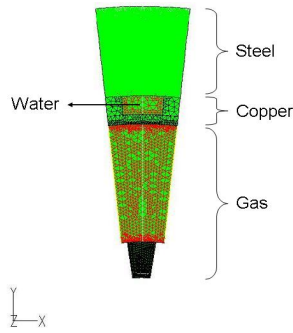
Figure 3.13: Meshed Exit View of the Fluid-Thermal Model.

The fluid-thermal analysis was done using Fluent®. Fluent® is a computational fluid dynamics (CFD) code which solves the equations for conservation of mass, momentum, energy using the finite volume method. It was used mainly for obtaining thermal heat transfer data (fluid-solid coupling) in this analysis. The Three-dimensional, Segregated, Implicit, Unsteady solver settings in fluent were activated for the problem in hand. The segregated implicit solver, used for solving the complete set of coupled equations for all the control volumes, is a general preferred solver since it requires lower memory requirements than the coupled implicit solver and also provides more flexibility in the solution procedure. A relative velocity formulation and a cell based gradient option was used for the analysis. A node based gradient option was also tried but it increased the run time slightly without producing significant variations in the solution.

The Spalart-Allmaras viscous model, a good model to use for high speed flows like those being studied here was used to obtain the solution. The Spallart-Allmaras model is a single equation model for the turbulent viscosity. Hence it is faster and uses lesser computational resources than the higher equation order solution methods. Spallart-Allmaras is a type of Reynolds Averaged Navier-Stokes (RANS) model. The viscous

heating option was also considered to account for the viscous flow heat generation in the boundary layer region.

To obtain a faster and more robust result, a first order discretization was used for the pressure, density, momentum, modified turbulent viscosity and energy solutions. The discretization is the method for interpolating results from the cell center to the faces. For better accuracy, a second order discretization was used for pressure. A second order upwind discretization for density, momentum, modified turbulent viscosity and energy. The SIMPLE method of discretization was used for pressure-velocity coupling. First order methods are more robust and the second order discretization gives more accurate results. The discretization methods can be used together if the second order discretization fails to converge. The SIMPLE method is an algorithm which uses a relationship between velocity and pressure corrections to enforce mass conservation and to obtain the pressure field.

The model consisted of both solid and fluid zones. The combustion chamber gas was modeled as an ideal gas, hence there were two fluid zones, ideal gas for the combustion gases and water for the coolant. There were also two solid zones consisting of copper walls in between the gas and coolant side and steel for the closeout. All active equations are solved in the fluid zone while only heat conduction equations, i.e no flow equations are solved for in the solid zone.

Besides the standard fixed inputs for the solids and fluids, the following temperature dependent properties were also used to model material behavior under different temperature, pressure and velocity conditions. Fluent® uses a polynomial function input for field variable dependent material properties. Thus a polynomial function was created

and used for the necessary material properties. For this analysis the polynomial functions for the constituent material properties specific heat, C_p, and thermal conductivity, K, are:

Air:

$$C_p = 931.59 + 0.2082T \tag{3.1}$$

$$K = 0.0089 + (6e - 05)T \tag{3.2}$$

Water:

$$C_p = 5476.9 - 8.1871T + 0.0129T^2 \tag{3.3}$$

$$K = -0.59 + 0.0067T - (9e - 06)T^2 \tag{3.4}$$

Copper:

$$C_p = 377.33 + 0.1565T + (4e - 05)T^2 - (1e - 07)T^3 \tag{3.5}$$

$$K = 411.7 - 0.0962T + (5e - 05)T^2 \tag{3.6}$$

Steel:

$$C_p = 337.86 + 0.4716T - (2e - 04)T^2 \tag{3.7}$$

$$K = 12.111 + 0.0127T \tag{3.8}$$

Pressure inlet and outlet boundary conditions were used in the analysis for both the gas zone and the water zone. The pressure input at the gas inlet, based on the
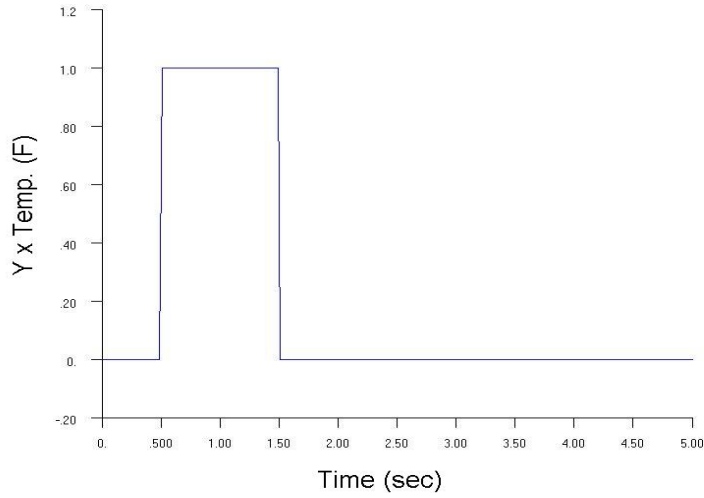
Figure 3.14: Temperature Firing Cycle.

experimental model, was 215 psi with atmospheric conditions existing at the outlet. The coolant water, based on the experimental model, had an input pressure of 100 psi and outlet of 85 psi. The input temperature of the gases based on experimental results was approximately 3441°F. To help convergence in Fluent®, the absolute pressure can be separated into the gage pressure and operating pressure. In this analysis, since there were no convergence problems, the operating pressure was kept as zero so that the gage pressure for the inlet and outlet refer to the absolute pressure. The coolant water had steady pressure and temperature inlet conditions while the gas pressure and temperature followed a firing cycle pattern at the inlet. The firing pattern at the gas inlet is shown in figure 3.14.
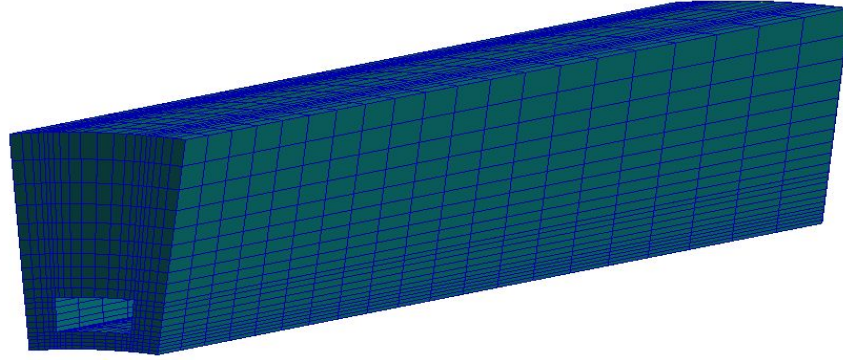
Figure 3.15: Meshed View of the Thermo-Structural Model.

3.3 Thermo-Structural Analysis Model

The structural model was constructed using the pre-processor MSC/Patran® with the MSC/Marc® template. Initially, the analysis was performed using a coarse mesh and later refined using one-way and two-way bias mesh seeding to construct a finer mesh at the higher strain regions. The mesh used was a completely structured mesh consisting of three-dimensional hexagonal elements. The mesh consisted of 7200 elements and 8757 node points. Cyclic symmetry boundary conditions were used to accurately model the symmetric nature of the section. The thermo-structural model is shown in figures 3.15 and 3.16. Figure 3.15 shows an isometric view of the mesh from the outlet side, while the sectional view is displayed in figure 3.16.
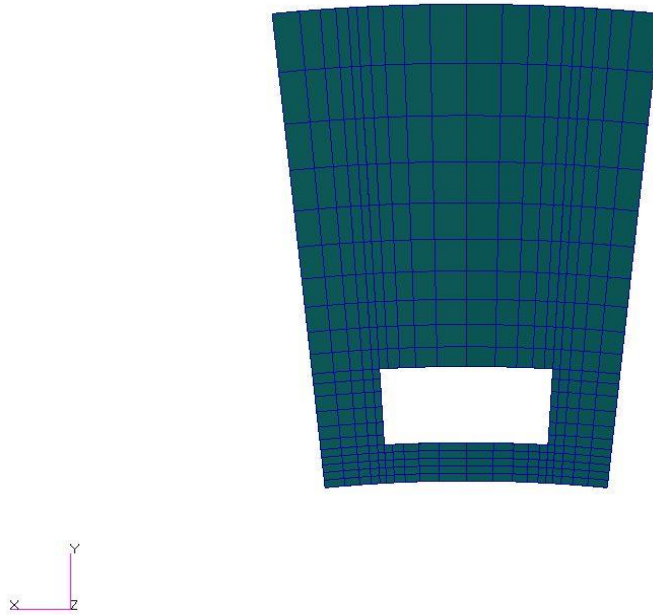
Figure 3.16: Meshed Sectional View of the Thermo-Structural Model.

The chamber materials are subject to high temperatures and pressures of a cyclic nature during the operation of the thrust chamber. Thus the presence of temperature dependent material properties and material non-linearities must be considered during the analysis. The thermo-structural analysis was performed using a non-linear solver, MSC/Marc®, due to the presence of these material nonlinearities.

Temperature and pressure output from the fluid-thermal analysis were used as inputs into this analysis. Transient inputs were available from the fluid-thermal analysis. The thermo-structural analysis used results from the transient solution from FLUENT® to establish individual static loadcases. This approach was used since the temperature and pressure inputs were known as a function of time. Multiple entries of fixed time steps of a second were used to construct static loadcases and were run sequentially to

28

approximate the time dependent nature of the forcing functions. It should be noted that a thermal diffusion analysis was also performed since temperatures from the fluid-thermal analysis were obtained only at the bottom gas wall surface and the coolant wall surfaces. The thermo-structural analysis determined the temperature distribution for the entire structural model.

A multifrontal sparse solver was used in Marc to decompose the stiffness matrix. The multifrontal sparse method is one of the more efficient computational methods. The multifrontal sparse method is a direct sparse method of decomposing matrices. A Newton Raphson scheme was used for time integration. A fixed load step of 0.01 of the total load was chosen for each firing cycle. A load step of 0.05 was chosen for the steady state loadcases. The Cuthill-McKee method was used for bandwidth optimization.

Only copper and steel material properties are needed in the thermo-structural analysis. OFHC copper and AISI 304 steel were the materials used to construct the subscale rocket engine thrust chamber at Purdue. High temperatures lead to high thermal stresses which have to be relieved, thus selecting a material with high thermal conductivity such as oxygen free high conductivity (OFHC) copper is necessary so that the coolant can take away most of the heat. Steel plays the part of the coolant channel closeout where the material has to have high structural strength to sustain the large pressures occurring in the chamber and avoid failures such as buckling. The stainless steel also has anti-corrosion properties which can help with the expected corrosion after repeated firings in the combustor. The properties of these metals vary with temperature and the data used for temperature dependency are shown in figures 3.17 to 3.22. Figures 3.17 and 3.20 show the specific heat variation of copper and steel with temperature. The specific heats of copper and steel increase with an increase in temperature. Figure 3.18 and 3.21 show
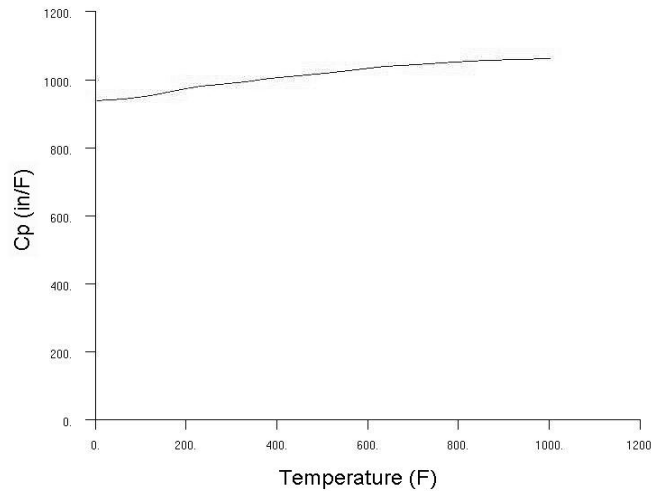
Figure 3.17: Variation of Specific Heat of copper with Temperature.

the variation of the elastic modulus for copper and steel with temperature. The elastic moduli of both decrease with increasing temperature. Figures 3.19 and 3.22 show the variation with temperature of the thermal conductivity of copper and steel respectively. The thermal conductivity of copper decreases with increase in temperature while that of steel increases with increase in temperature.

A combination of elastic and plastic constitutive models were used to model the material behavior. This allows for the determination of the irreversible straining that occurs in a material once a certain level of stress is reached. Plastic strains are assumed to develop instantaneously, independent of time. Plasticity theory thus provides a mathematical relationship that characterizes the elastoplastic response of materials. The plastic constitutive model can be defined using the type, hardening rule, yield criteria and strain-rate method components. The yield condition, flow rule and hardening

30

Young's Modulus of Elasticity Vs. Temperature for Copper
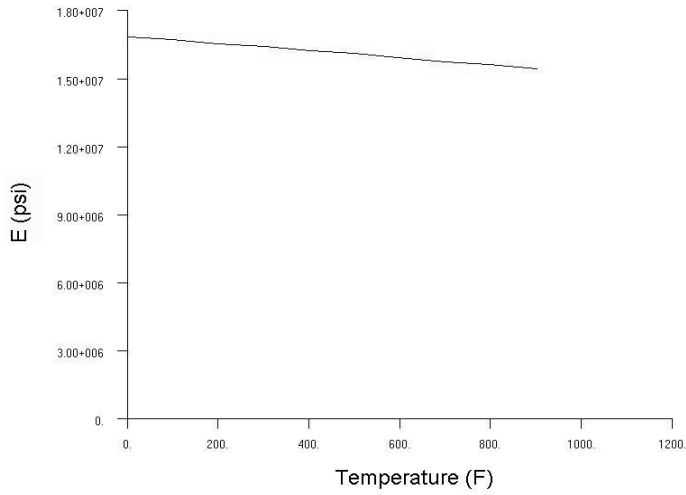
Figure 3.18: Variation of Elastic Modulus of copper with Temperature.
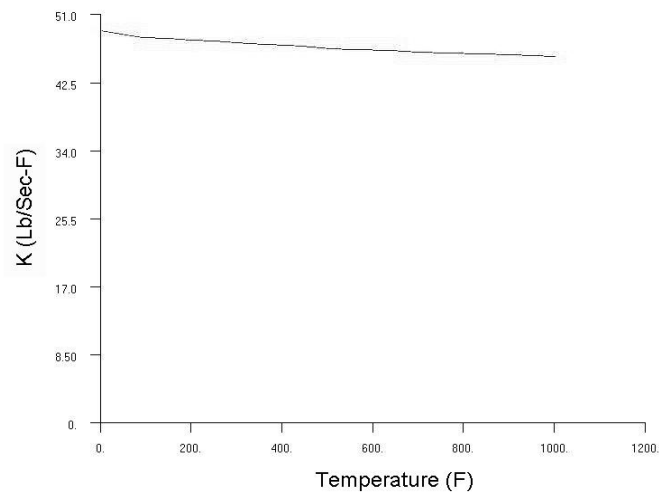
Thermal Conductivity Vs. Temperature for Copper

Figure 3.19: Variation of Thermal Conductivity of copper with Temperature.
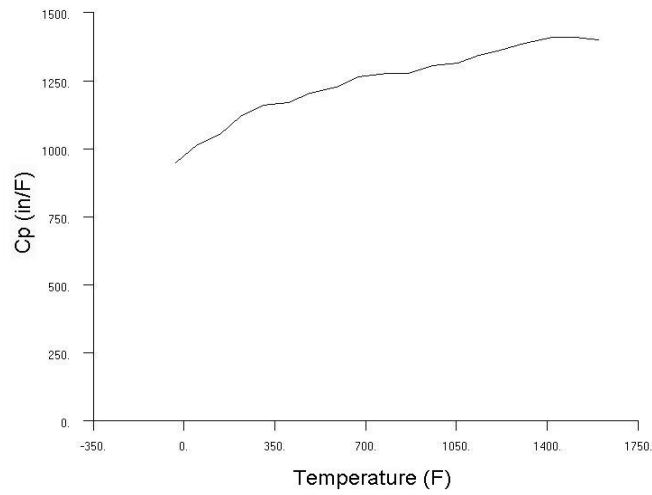
31

Specific Heat Vs. Temperature for Steel

Cp (in/F)

Temperature (F)

Figure 3.20: Variation of Specific Heat of steel with Temperature.
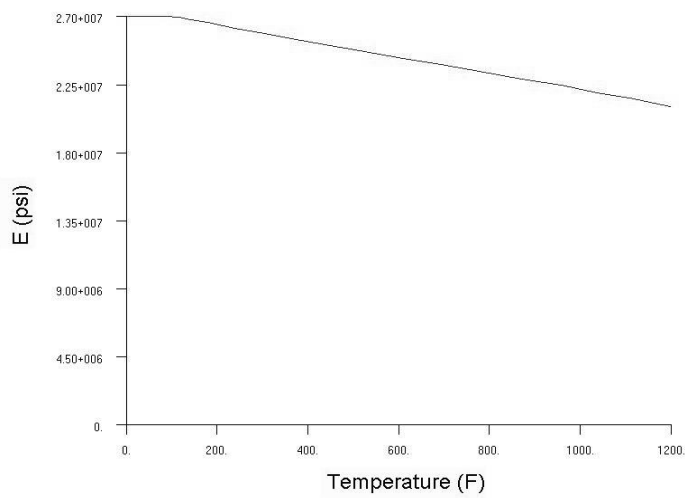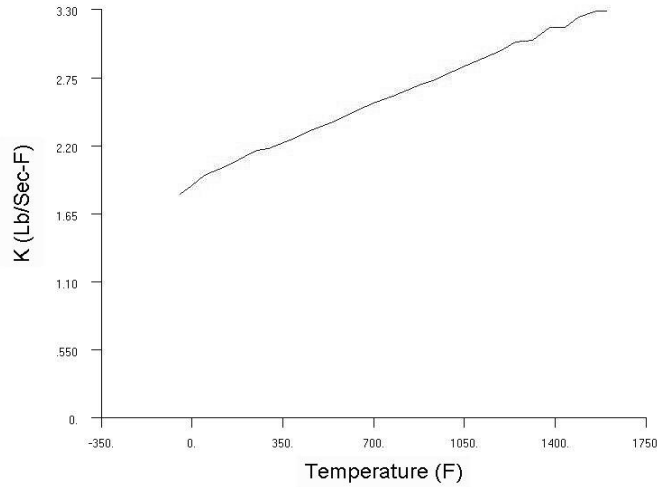
Young's Modulus of Elasticity Vs. Temperature for Copper

E (psi)

Temperature (F)

Figure 3.21: Variation of Elastic Modulus of steel with Temperature.

Figure 3.22: Variation of Thermal Conductivity of steel with Temperature.

rule are necessary to calculate the stress and plastic strain. The hardening rule describes the change in the yield surface with progressive yielding, so that the stress states for subsequent yielding can be established. The isotropic hardening rule was used for the analysis. In isotropic hardening, the yield surface remains centered about its initial centerline and expands in size as the plastic strains develop. For materials with isotropic plastic behavior, this is called isotropic hardening. The yield criteria determines the stress level at which yielding is initiated. The von Mises yield criteria was used for the analysis performed. If the equivalent stress computed using elastic properties exceeds the material yield, then plastic straining occurs. Plastic strains reduce the stress state so that it satisfies the yield criteria. Also, the yield criteria changes with hardening. A Piecewise-Linear strain rate method was used to calculate the plastic strain increment inclusive of the dependencies mentioned. The size of the plastic strain increment
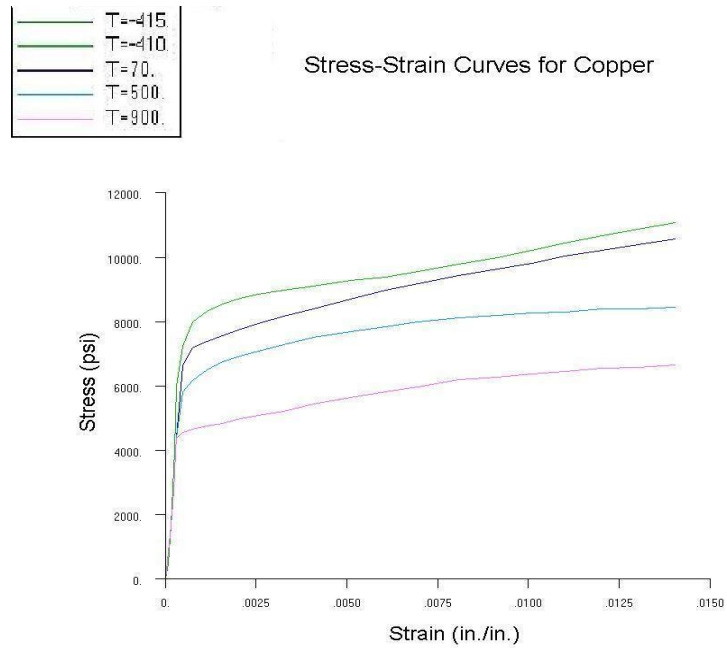
33

Figure 3.23: Stress-Strain Curves of copper with Variation in Temperature, Elastic and Plastic Region.

is therefore related to the total increment in strain, the current stress state, and the specific forms of the yield surface.

The stress-strain curves for copper and steel are as shown in figures 3.23 to 3.26. Figure 3.23 and 3.25 show both, the elastic and plastic region while figures 3.24 and 3.26 only show the plastic region. These are necessary to obtain results when the material goes into the plastic region in which the stress and strain are not directly proportional, that is they are not linear. Hence the code directly obtains the required values form these curves.

The structural model was fixed on the inlet side representing the thrust chamber being bolted to the combustor. Symmetric boundary conditions were applied to the side walls of the model since only a 12° section containing one coolant channel of the total 30 in the 360° geometry was modeled.
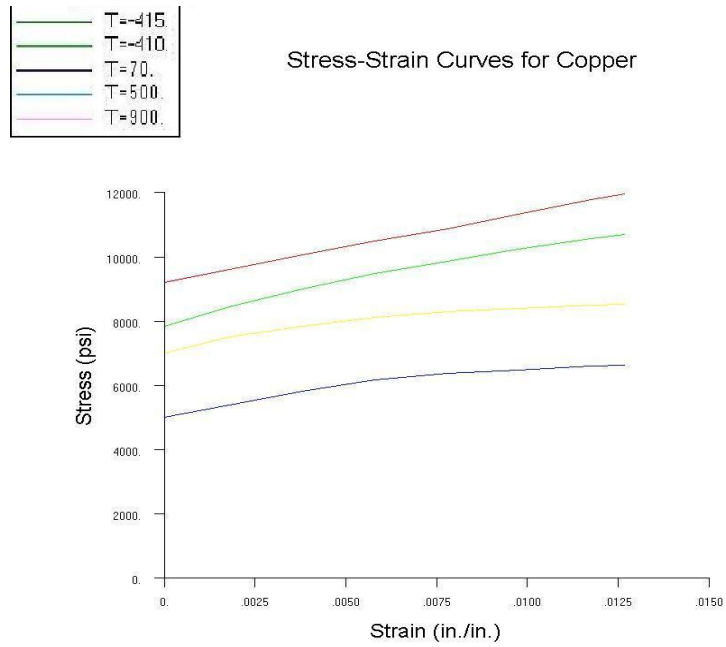
Figure 3.24: Stress-Strain Curves of copper with Variation in Temperature, Only the Plastic Region.
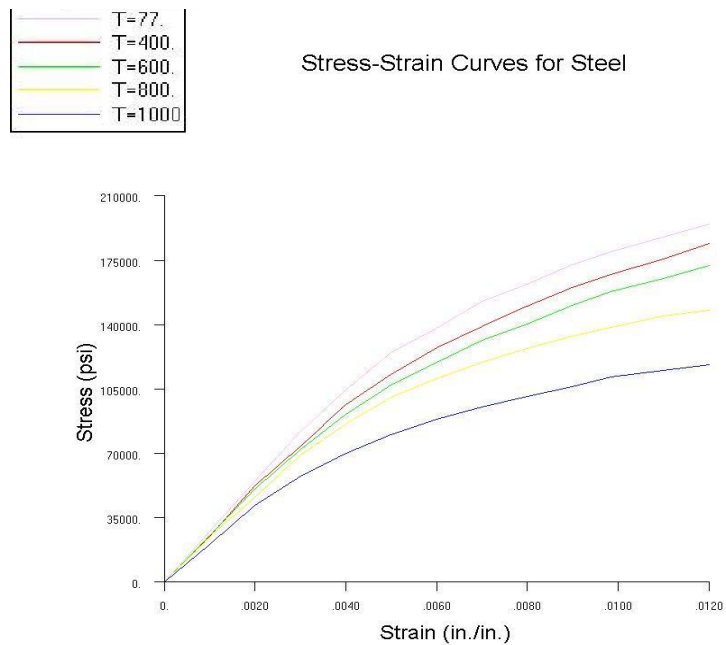
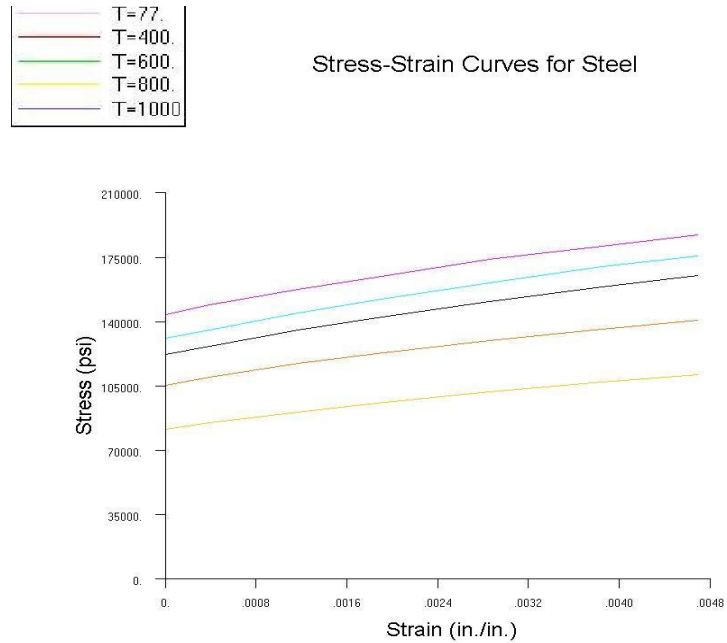Figure 3.25: Stress-Strain Curves of steel with Variation in Temperature, Elastic and Plastic Region.

Figure 3.26: Stress-Strain Curves of steel with Variation in Temperature, Only Plastic Region.

The loads for the thermo-structural part consisted of tabular pressure and temperature inputs to the model. The pressures are constant in the X direction of the model at the gas and coolant surface while it varies in the Z direction. The temperatures also vary in the Z direction at both the gas side and coolant side walls, they are constant in the X direction at the gas side wall but vary in the X direction at the coolant walls. These temperature and pressure loadings on the model are explained in detail in chapter 4.

Results

The results obtained from the three-dimensional fluid-thermal-structural analysis of the subscale thrust chamber were compared to the experimental and finite element analyses presented by Sung et al.[1]. The finite element analyses performed by Sung et al. were two-dimensional non-linear structural analyses.

From the three-dimensional transient fluid-thermal analysis a maximum temperature of 597 K (615 F) was obtained for the copper gas side wall surface. This was less than the estimate obtained by Sung et al. of 670 K from a steady state analysis. Sung et al. calculated this estimate using the coolant temperature obtained from the experimental analysis and using a simple one dimensional Bartz and Seider-Tate equations for the hot gas and coolant side heat transfer coefficients to calculate the temperature variation. This could be explained by the fact that smooth wall surfaces were modeled in this analysis. Surface roughening on the chamber walls increases heat transfer from the hot gas to the chamber wall[15]. A higher coolant outlet temperature compared to the experimental result, as shown later, could also be a possible reason for the lower temperatures observed since it implies that more heat was absorbed by the coolant in this analysis than that observed in the experimental analysis. Heat transfer due to radiation from the gas though possibly very small is also a factor which was not considered during the analysis stage. The results obtained from the transient fluid thermal analysis and the profile estimated by Sung et al. at the gas side copper wall along the length of the chamber are compared in figure 4.1. It was observed that the temperature rise in the
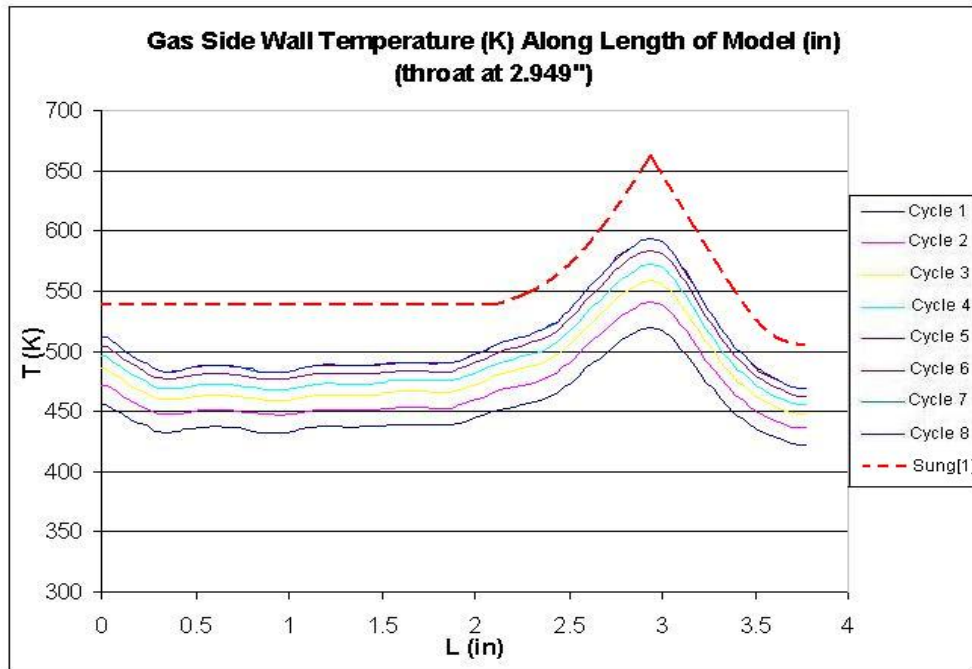
Figure 4.1: Temperature Variation At Gas Side Wall Along Length of Model for the First Eight Firing Cycles, Fluid-Thermal Analysis and Sung's[1] Analysis.

initial portion of the chamber wall was small but it increases in the converging part of the nozzle and is maximum at the throat. The temperature decreases in the diverging part of the nozzle. It was also seen that although the temperature profile remained similar for all firing cycles the magnitude of the temperatures increased for the first few firing cycles and eventually reached a state where the rise in temperatures was very small for successive firing times. It was inferred from this that a steady state was reached and that future cycles would not show significant variation in temperatures at the wall.

The coolant temperature at the outlet obtained from the fluid-thermal analysis was around 348 K (167 F) compared to the experimental output of 341 K (154 F) obtained by Sung et al. The value was slightly higher but matched well with the experimental results obtained. A possible reason for the higher temperature is that, in the experimental
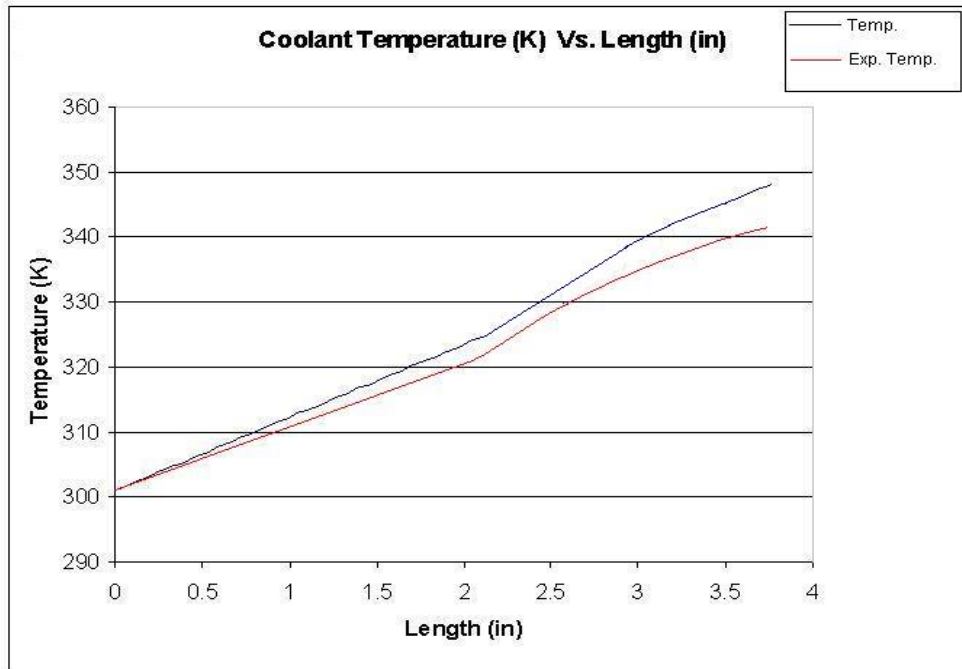
Figure 4.2: Coolant Temperature Rise Along Length of Model, Fluid-Thermal Analysis.

analysis the pressure fluctuates above and below the uniform pressure value used in this analysis causing changes in the heat transfer rates. The results are compared in figure 4.2. A steady rise in temperature was seen in the cooling channel fluid as it flows from the inlet to the outlet of the channel. This can be seen in figure 4.2, where the left and right sides refer to the coolant inlet and outlet respectively. The rate of rise observed in the convergent region of the model was slightly higher then the other regions. By comparing the two plots it can be seen that similar behavior was also observed in the experimental analysis.

The contours for temperatures at the first and eighth firing cycles are as shown in figures 4.3 and 4.4. The remaining contours can be referred to in appendices A and B. The effectiveness of the cooling fluid could be seen by the variation in temperatures in the copper liner and the steel close-out. The copper liner is the part which forms the
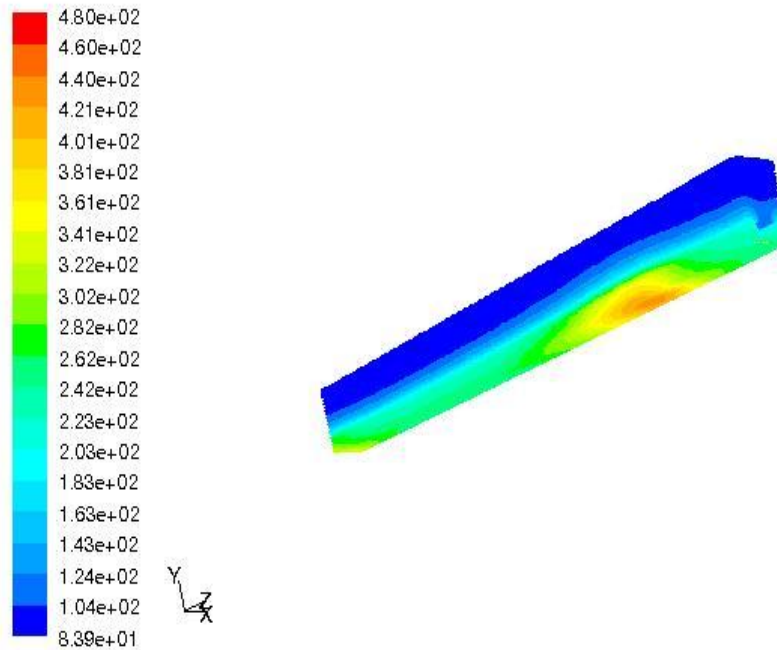
Figure 4.3: Temperature Contour in the Solid Zone After the First Firing Cycle.

wall on the gas side of the chamber while the steel acts as the backing to the coolant channel. The coolant flows in between the copper liner and the steel close-out. The temperatures observed in the copper liner were far higher than those seen in the steel close-out. The temperatures in the copper liner and steel close-out were observed to increase in the convergent region and was the highest at the throat implying maximum heat transfer from the gas to the wall in this region.

The temperatures at the throat as a function of time are shown in figure 4.5. The plot shows the increase in the temperature at the throat section as the number of firing cycles go on increasing. The rise rate in temperature was higher at the initial cycles but decreased and reached a near steady state value of 597 K (615 F) after about 6 firing cycles. The rise in temperature after that was very small as seen in the difference in the
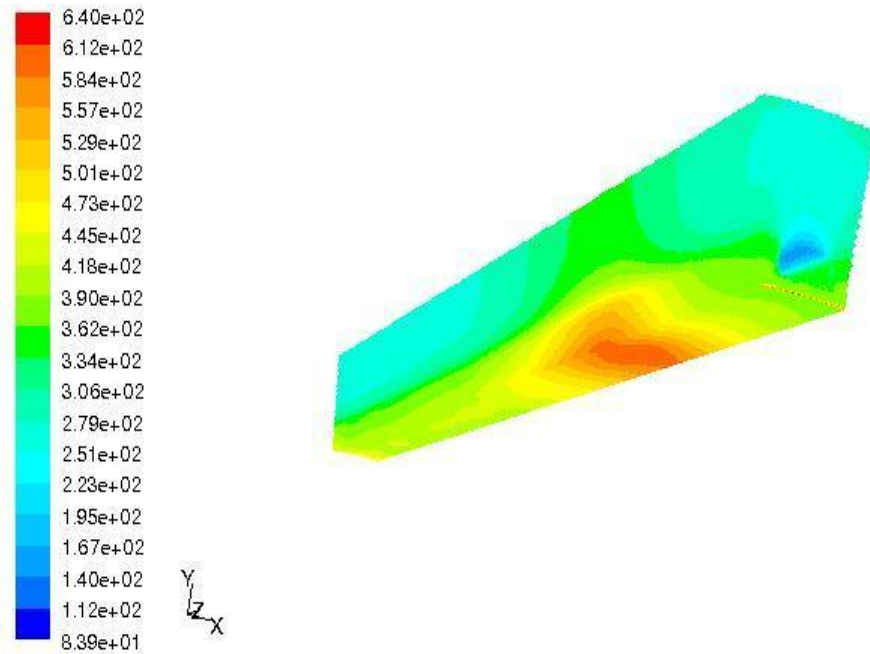
Figure 4.4: Temperature Contour in the Solid Zone After the Eighth Firing Cycle.

maximum temperature between the 6th and 7th and 7th and 8th firing cycles. The same steady behavior will continue for the later firing cycles too.

The pressure load variation on the gas and water side are shown in figures 4.6 and 4.7. The gas pressure dropped slightly over the straight portion of the chamber while the pressure drop was large in the converging part towards the throat region and leveled out again in the diverging section of the nozzle. This kind of pressure variation is typical in convergent-divergent nozzles. The inlet gas pressure at the head end was 215 psi and the pressure at the outlet was about 31 psi. The water pressure shows a pressure drop across the length of the cooling channel. The coolant inlet pressure was 100 psi while the outlet pressure observed was 88 psi.

The temperature and pressure loads determined above were then used to calculate the stress, strain and displacements in the model. The total strain in the Y direction

41
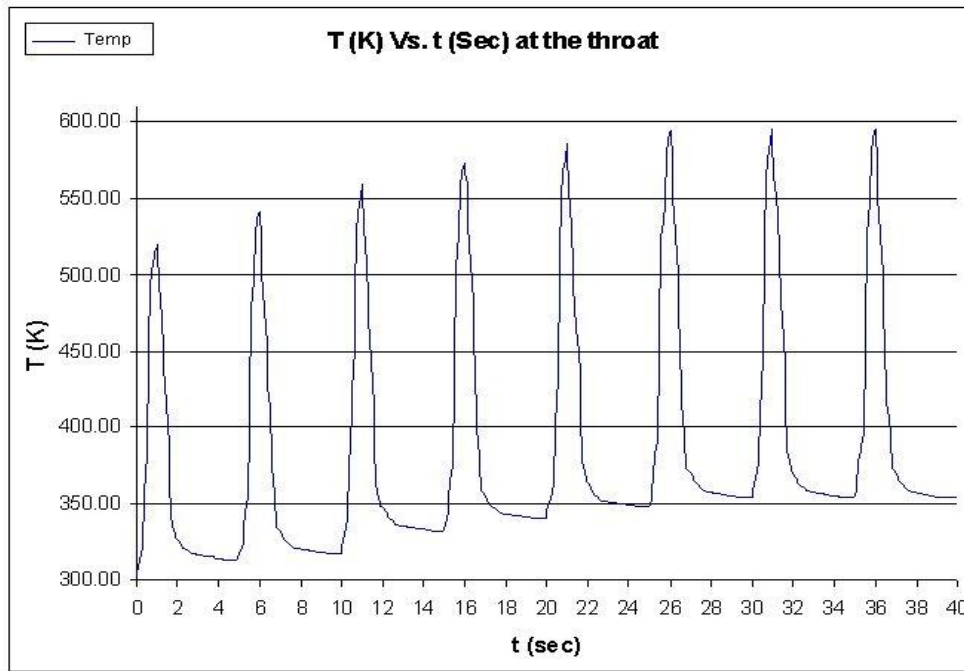
Figure 4.5: Temperature Variation at the Throat Gas Side Wall Over 8 Firing Cycles
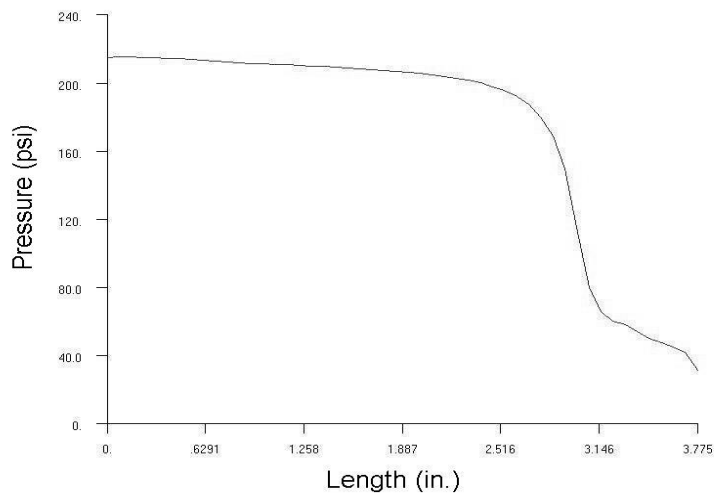
Figure 4.6: Pressure Variation Along The Gas Side Wall (+Z).
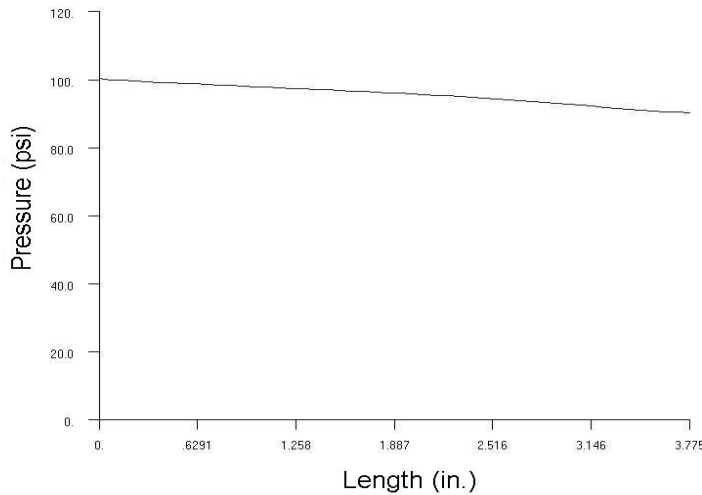
Figure 4.7: Pressure Variation Along the Water Wall Faces (+Z).

for the model at the 1st and the 20th firing cycles are as shown in the figures 4.8 and 4.9. The complete set of contours can be referred to in Appendices C and D. The total strain in this analysis is defined as the sum of the elastic, plastic and thermal strains. The maximum total strain was observed in the Y direction for this analysis and was the strain value considered for life determination. The total Y strain was also the parameter considered in Sung's[1] analysis, hence enabling the values obtained in this analysis to be directly compared to it.

A large increase in the strains was observed during the firing times and the copper liner material went into the plastic region in the first few firing cycles. During the cool down stages or the non-firing times the strain values of the liner, though still in the plastic range were significantly smaller. i.e, the strain behavior followed the highs and lows similar to that of the temperature loading pattern. Due to its constricting the

43
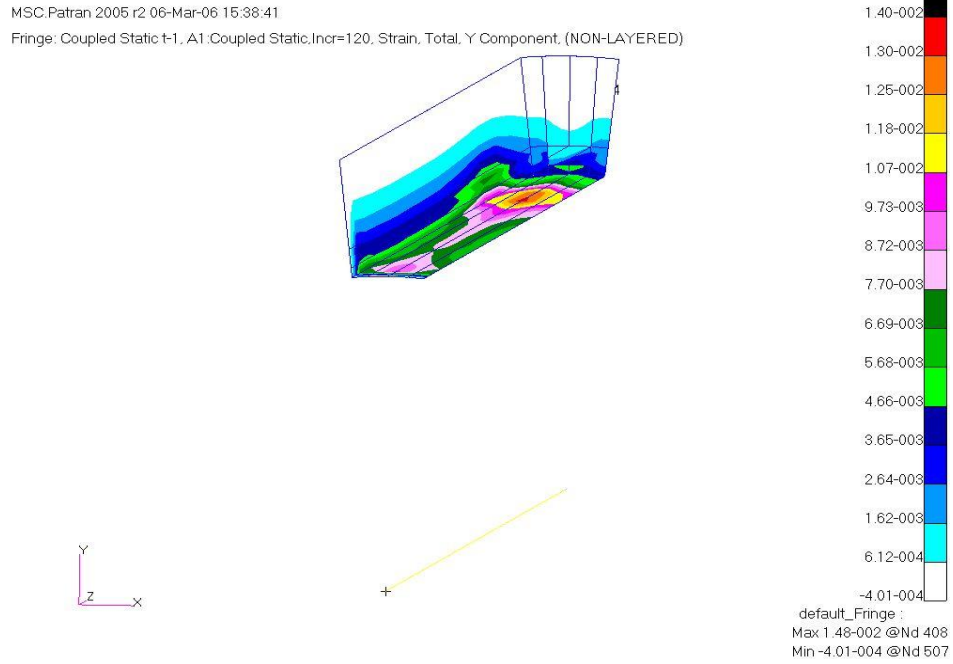
Figure 4.8: Contour of Total Strain in the Y Direction After the First Firing Cycle
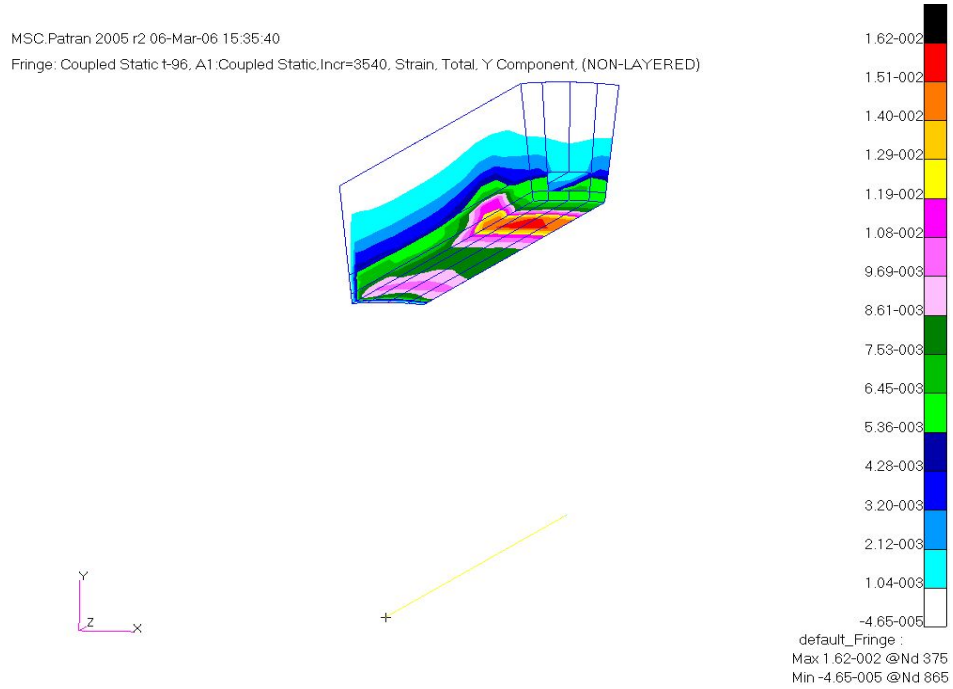
Figure 4.9: Contour of Total Strain in the Y Direction After 20 Firing Cycles
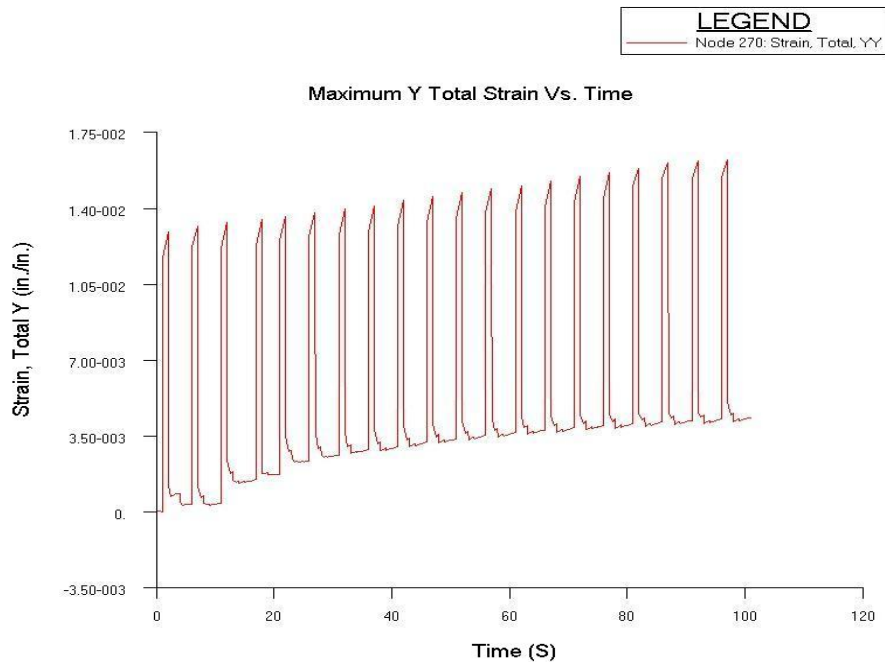
Figure 4.10: Total Y Strain Variation for 20 Firing Cycles at the Throat Section

expansion of the copper liner, the steel close-out also went into the plastic region with the largest plastic strain at the copper and steel interface. These strains in the steel were small compared to the liner material. The variation of total Y strain with time at the throat section where maximum strains were observed is shown in figure 4.10. The rate of increase in the strain magnitudes was higher at the first few firing instances but the increase in maximum strain gradually decrease and after about 20 firing cycles this increase was very small compared to the 18th and the 19th firing cycle. The maximum value of the total strain in the Y direction after 20 firing cycles, i.e after an analysis time of 96 seconds was 0.0162 in/in in the copper liner as seen in figure 4.9. Since no substantial rise in the strain values were observed at these times, the obtained values for strain were considered to estimate the life of the chamber using the strain-life curve for OFHC copper. The reason for using the strain life estimation was that in fatigue

problems where the stress is high enough for plastic deformation to occur, failure occurs due to low cycle fatigue. Strain based life estimate predictions are used for low cycle fatigue problems. Stress based life estimation is generally used for high cycle fatigue problems, where the material stays in the elastic region. Low cycle fatigue is generally defined as fatigue when the cycles to failure are less than 10^3, while for high cycle fatigue, the cycles to failure is between 10^4 and 10^8 [32]. The maximum Y total strain as seen in figure 4.8 and 4.9 was observed at the throat section of the copper wall between the gas side and coolant side. It was also observed that the plastic strain constitutes the major strain in the initial firing cycles, 0.0105 in/in of a total strain of 0.0138 in/in. Plastic strain is the nonrecoverable or permanent strain obtained after removing a load greater than the elastic limit of the material on which it is applied. In the latter firing cycles when the temperature at the wall was much higher the thermal strain induced in the copper region was nearly equal to the plastic strain. So, these two make up most of the total strain while the elastic strain at both the initial and final stages is a small amount of the total strain, 0.00061 in/in and 0.00198 in/in respectively. The elastic strain is a recoverable or reversible strain. So, once the loads are removed this portion of the strain goes to zero.

A comparison was made with these results and the results obtained by Sung's [1] two-dimensional analysis and the following observations were made. As seen in figure 4.11, Sung et al. obtained a total strain of 0.02 in/in using a two-dimensional ANSYS® model which led to a life estimation of 115 cycles for the chamber liner. They also performed a two-dimensional analysis using ABAQUS®, refer figure 4.12, and obtained a maximum strain of 0.012 in/in at the throat section which led to an estimated life of 320 cycles. The MSC/Marc® three-dimensional model for this project gave a maximum strain of 0.0162
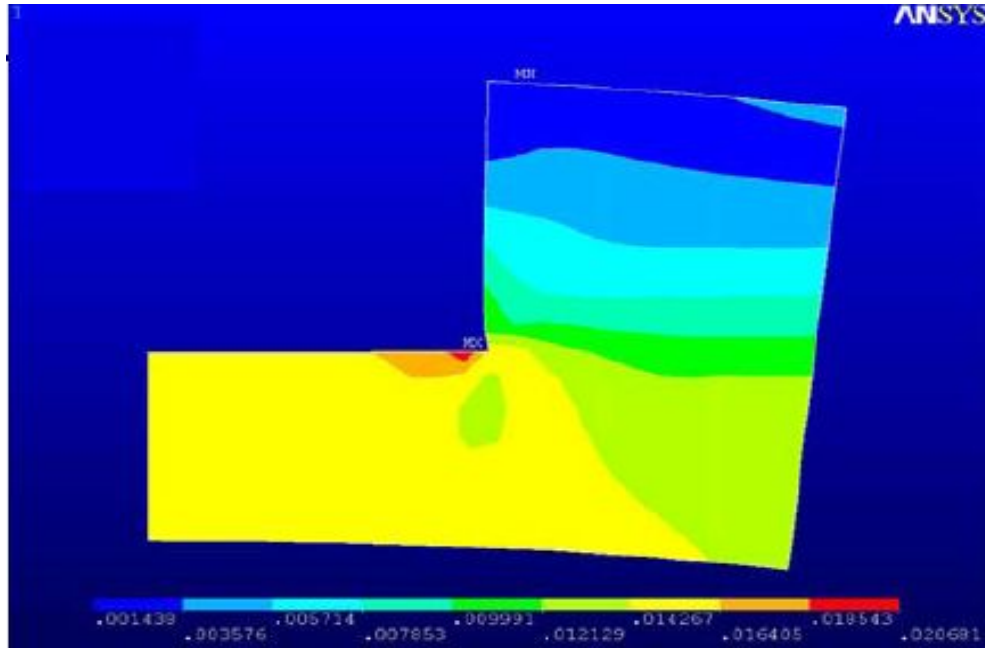
Figure 4.11: Total Strain of 2% Obtained Using a Two-Dimensional ANSYS Analysis, Anderson[21] et al. (2003).

in/in at the center of the ligament of the throat section copper liner as seen in figure 4.9. Based on this strain value a life of 255 cycles was estimated. This estimate gave better agreement with the number of cycles to failure obtained in the experimental analysis. The strain-life curve for OFHC copper was used to calculate the life and is shown in figure 4.13. The strain contours obtained by Sung et al. can be seen in figures 4.11 and 4.12, while the maximum strain contour obtained in this study is given in figure 4.9.

In the X direction, the maximum value of total strain was obtained at the throat section on the side walls of the coolant channel and was small in comparison to the Y strain obtained at the bottom copper wall. The maximum stress on the chamber was found out to be 75.1 ksi at the end of the 20th firing cycle and was about 48.4 ksi at the end of the first firing cycle. These high stresses were observed at the fixed end and at
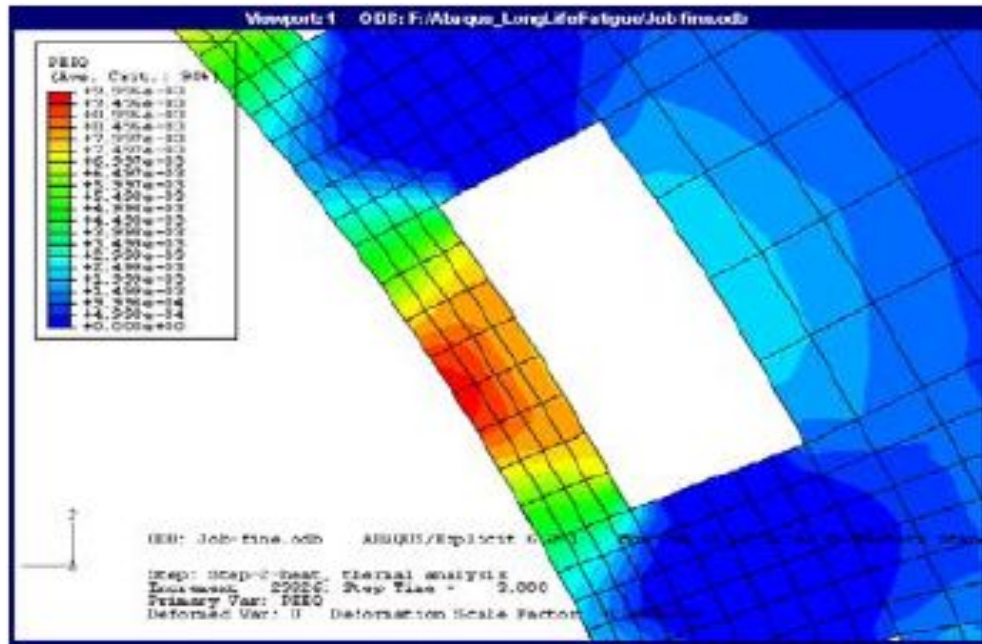
Figure 4.12: Total Strain of 1.2% Obtained by Using a Two-Dimensional ABAQUS Analysis, Anderson[21] et al. (2003).
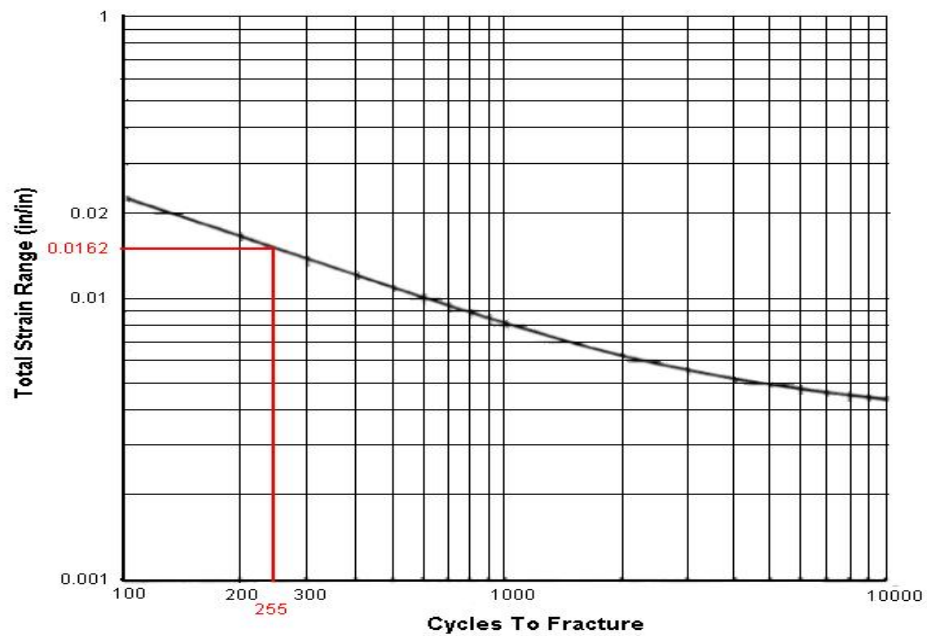
Figure 4.13: Strain-Number of Cycles to Fracture Curve for OFHC copper, Esposito and Zabora[11] (1975).

Table 4.1: Comparison of Life Cycle Predictions Made using the Various Methods discussed.

Prediction Method	Estimated Life (No. of Cycles)
Experimental Analysis	270
The Two-Dimensional ANSYS Analysis	115
The Two-Dimensional ABAQUS Analysis	320
The Three-Dimensional MSC/Marc Analysis	255

the throat region of the inner steel closeout wall. The strains, displacements and stresses at the 1st and the 20th firing cycles are shown in appendices C and D.

A comparison of the life estimates obtained for the modeled thrust chamber using the various methods discussed above are summarized in table 4.1.

CHAPTER 5

CONCLUSIONS

A successful three-dimensional transient fluid-thermal-structural nonlinear analysis was performed to estimate the maximum number of firing cycles for a subscale rocket engine thrust chamber before failure occurs. The maximum strain was obtained at the throat section of the oxygen free high conductivity copper liner which separates the combustion gas side and the coolant water side. The fatigue curve for the liner material was used to estimate the life of the chamber since it would fail first. A life of 255 cycles was estimated based on this procedure. The experimental analysis performed on the same model failed after 270 cycles due to excessive strains at the midsection of the copper liner similar to that observed in this coupled numerical analysis. The three-dimensional analysis showed better agreement than the two-dimensional analysis in predicting the life cycle failure when both low cycle fatigue and elevated temperature loads were applied.

BIBLIOGRAPHY

[1] I.-K. Sung, B.G. Northcutt, K.S. Rubel, W.E. Anderson, "A Subscale-Based Life Prediction Methodology For Rocket Engine Combustors," School of Aeronautics and Astronautics, Purdue University, West Lafayette, Indiana.

[2] W.E. Anderson, "Engine Design Drawings for A AE 590A Engine Life Prediction (Low Cycle Fatigue)," School of Aeronautics and Astronautics, Purdue University, West Lafayette, Indiana.

[3] R.J. Quentmeyer, "Experimental Fatigue Life Investigation of Cylindrical Thrust Chambers ," presented at the AIAA Thirteenth Propulsion Conference, Orlando, FL, July 11-13, 1977. NASA TM X-73665

[4] R.S. Jankovsky, V.K. Arya, J.M. Kazaroff, G.R. Halford, "Structurally Compliant Rocket Engine Combustion Chamber-Experimental and Analytical Validation," Journal of Spacecraft and Rockets, Vol. 32, No. 4, pp. 645-652, 1995.

[5] H.J. Kasper, " Thrust Chamber Life Prediction," NASA CP-2372, pp 36-43, 1984.

[6] J.S. Porowski, W.J. O'Donnell, M.L. Badlani, B. Kasraie and H.J. Kasper, "Simplified Design and Life Prediction of Rocket Thrust Chambers," AIAA Journal, Vol. 2, No.2, March 1985.

[7] X. Dai and A. Ray, " Life Prediction of the Thrust Chamber Wall of a Reusable Rocket Engine," Journal of Propulsion and Power, Vol. 11, No. 6, 1995.

[8] D.T. Butler, M-K. Pindera, " Analysis of Factors Affecting the Performance of RLV Thrust Cell Liners," University of Virginia, Charlottesville, Virginia, 2004.

[9] D. Zhu, U.S. Army Research Laboratory, Glenn Research Center, D.D. Fox and R. A. Miller, NASA, Glenn Research Center, L.J. Ghosn and S. Kalluri, Ohio Aerospace Institute, " Effect of Surface Impulsive thermal Loads on Fatigue Behavior of Constant Volume Propulsion Engine Combustion Materials," International Conference on Metallurgical Coatings of Thin Films, 2004.

[10] Armstrong, W. H. and Brogren, E. W. "'Thrust Chamber Life Prediction Volume II Plug Nozzle Centerbody and Cylinder Life Analysis"', NASA CR 134822, 1975.

[11] Esposito, J. J. and Zabora, R. F. "'Thrust Chamber Life Prediction Volume I Mechanical and Physical Properties of High Performance Rocket Nozzle Materials"', NASA CR 134806, 1975.

[12] Ellis, D. L. and Yun. H. M. ”‘Cu-8 Cr-4 Nb Alloy for Reusable Launch Vehicle Combustion Chamber Liners”’, Insights in R and T Presentation, April 13, 1999.

[13] Armstrong, W. H. and Brogren, E. W. ”‘3-Dimensional Thrust Chamber Life Prediction, NASA CR 134979”’, 1976.

[14] Armstrong, W. H., ”‘Structural Analysis of Cylindrical Thrust Chambers”’, NASA CR 159522, 1979.

[15] Hannum, N. P. and Price Jr., H. G. ”‘Some Effects of Thermal-Cycle-Induced Deformation in Rocket Thrust Chambers”’, NASA TP 1834, 1981.

[16] Robinson, D.N., and Arnold, S.M., ”‘Effects of State Recovery on Creep Buckling Under Variable Loading”’, Journal of Applied Mechanics, Vol. 57, 1990.

[17] Robinson, D. N. and Swindeman, R. W. ”‘Unified Creep-Plasticity Constitutive Equations for 2 Cr-1Mo Steel at Elevated Temperature”’, ORNL/TM-8444, 1982

[18] Arya, V. K. and Arnold, S. M., ”‘Viscoplastic Analysis of an Experimental Cylindrical Thrust Chamber Liner, NASA TM 103287, 1991.

[19] Freed, A.D., Verrilli, M.J. ”‘Viscoplastic Analysis of an Experimental Cylindrical Thrust Chamber Liner,”’ AIAA Journal, Vol. 30, No 3, 1992.

[20] R.S. Jankovsky, J.M. Kazaroff, ”‘A Life Comparison of Tube and Channel Cooling Passages for Thrust Chambers”’, JANNAF Propulsion Meeting,California, 1990.

[21] W.E. Anderson, J.C. Sisco, M.R. Long, and I.-K. Sung, ”‘Subscale Test Methods for Combustion Devices”’, Fifth International Symposium on Liquid Space Propulsion,Tennessee, 2003.

[22] ”‘Fluent 6.2 Users Guide Volume 2,”’, Fluent, 2001.

[23] ”‘MSC/Marc V 2005r2 User’s Guide,”’ MSC Software, 2005.

[24] ”‘MSC/Marc Volume A: Theory and User Information,”’ MSC Software, 2005.

[25] ”‘MSC/Marc Volume B: Element Library,”’ MSC Software, 2005.

[26] ”‘MSC/Marc Volume E: Demonstration Problems,”’ MSC Software, 2005.

[27] ”‘MSC/Marc Mentat Help Reference, MSC Software,”’ 2005.

[28] ”‘Introduction to Engineering Analysis using MSC/Marc and MSC/Patran V 2005r2, Seminar Notes Vol. 1, 2,”’ MSC Software, 2005.

[29] ”‘Introduction to Engineering Analysis using MSC/Marc and MSC/Patran V 2005r2, Seminar Workbook,”’ MSC Software, 2005.

[30] "'Metals Handbook, Vol. 1, Properties and Selection of Metals, Eighth Edition,"' American Society for Metals, 1961.

[31] Boyer, H.G., "'Atlas of Stress-Strain Curves,"' American Society for Metals, 1987.

[32] Bannantine, J.A., Comer, J.J., Handrock, J.L., "'Fundamentals of metal fatigue analysis ,"', Prentice Hall Publications, 1990.

[33] Patten, M.N., "'Information Sources in Metallic Materials,"' American Society for Metals, 1989.

[34] "'Material Behavior at Elevated Temperatures and Components Analysis,"' PVP - Vol. 60, American Society of Mechanical Engineers, 1982.

[35] DeGarmo, E.P., Black, J.T., Kohser, R.A., "'Materials and Processes in Manufacturing, Eighth Edition,"'1999.

[36] Bruhn, E.F., "'Analysis and Design of Flight Vehicle Structures,"' 1973.

[37] Roark, R.J., Young, W.C., "'Formulas for Stress and Strain,"' 1975.

APPENDICES

APPENDIX A

CONTOUR PLOTS FOR THE FLUID-THERMAL ANALYSIS AFTER THE FIRST FIRING

CYCLE
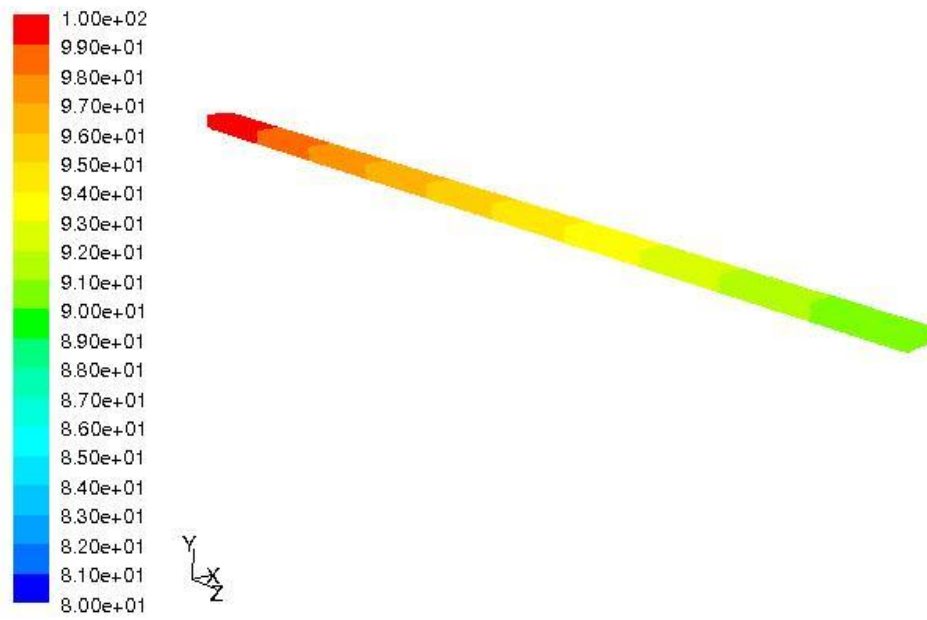
Figure A.1: Fluid Pressure Variation For the Water Region Along Length of the Model.
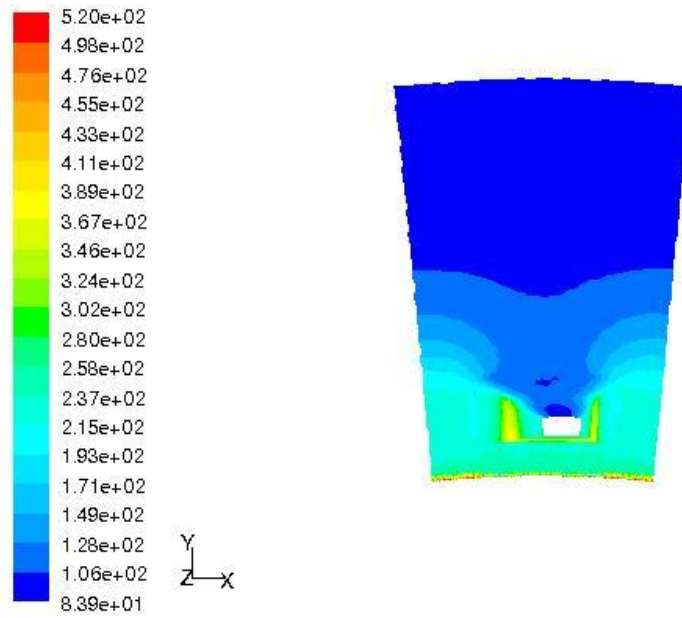
Figure A.2: Cross Sectional View of Temperature Variation at the Outlet.
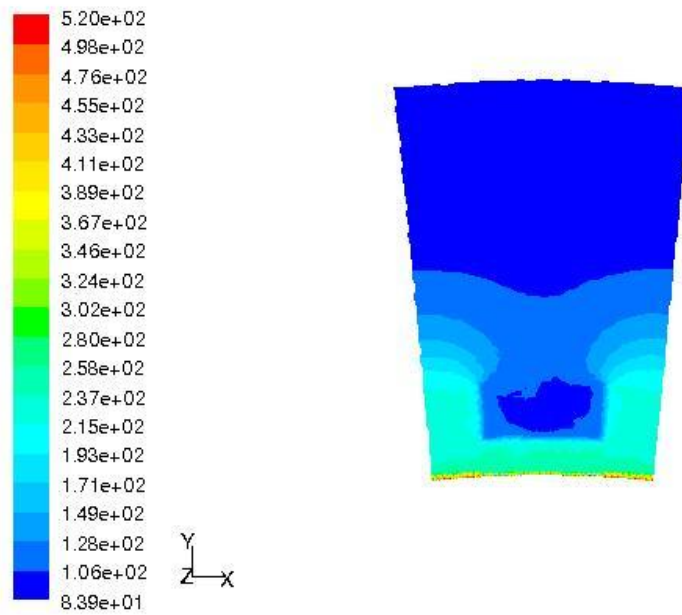
Figure A.3: Cross Sectional View of Temperature Variation at the Outlet Including the Water Region.
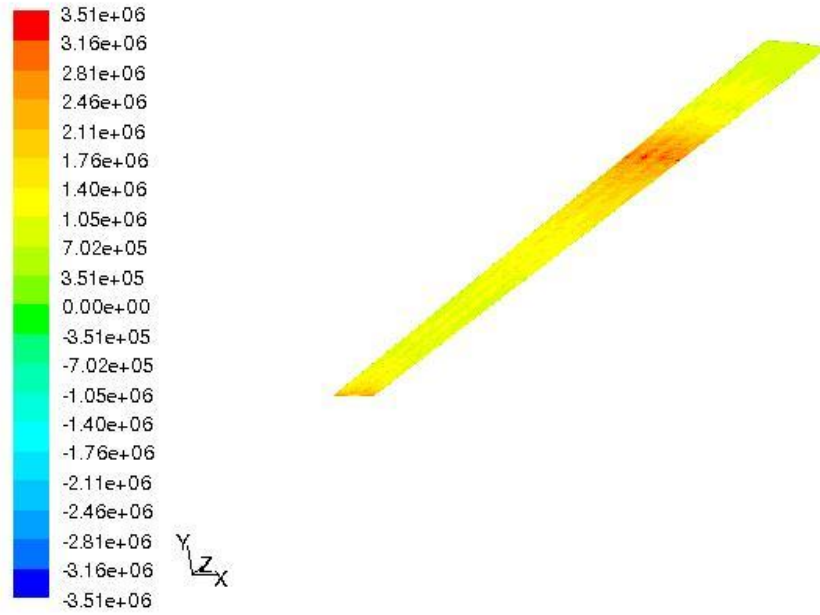
Figure A.4: Heat Flux Variation at Gas Side Wall Along Length of the Model.
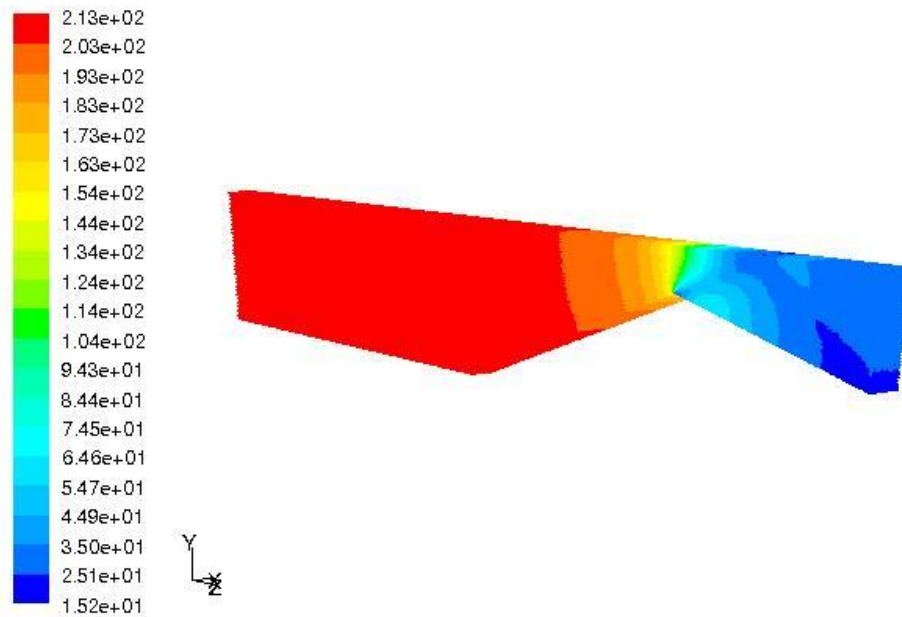
Figure A.5: Fluid Pressure Variation for the Gas Region Along Length of the Model.

57
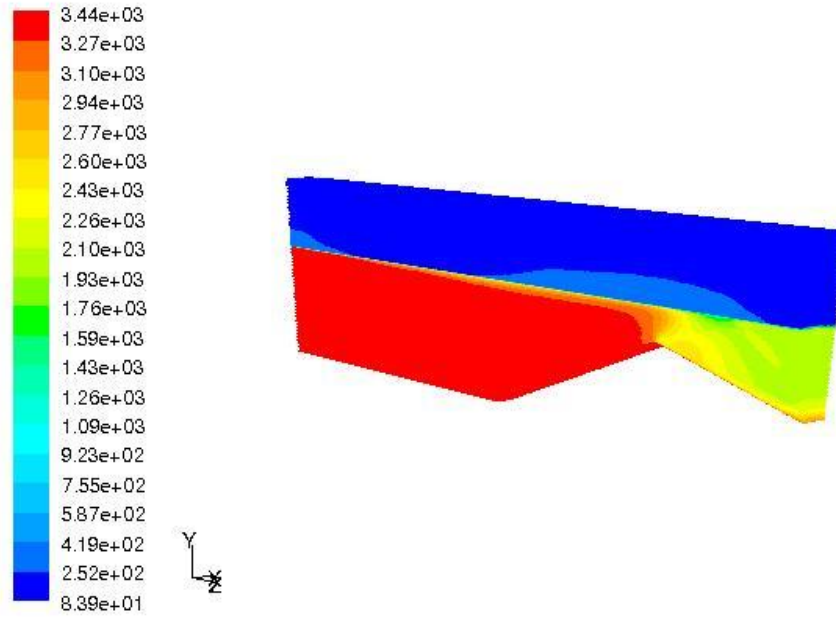
Figure A.6: Temperature Contours for All Fluid and Solid Zones in the Model.
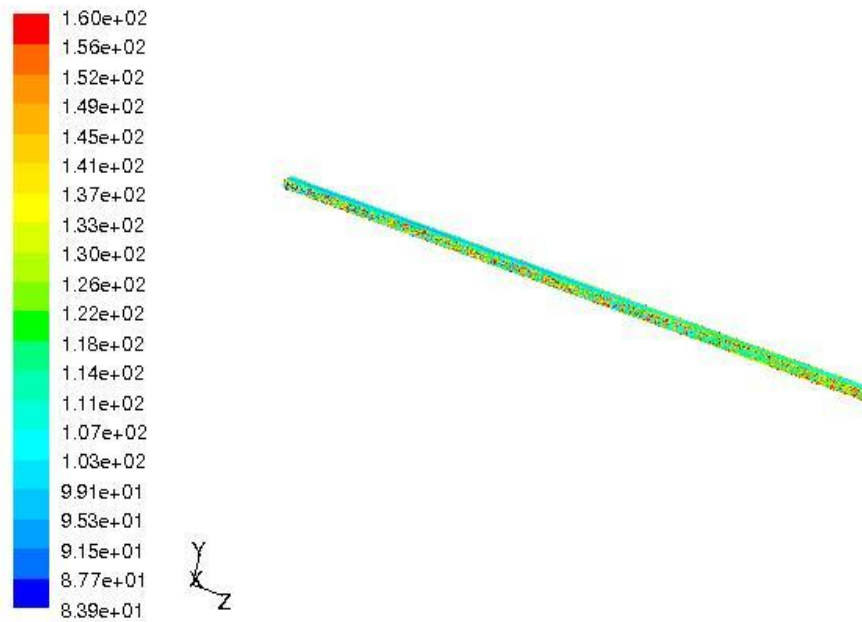
Figure A.7: Temperature Variation For Water Along Length of the Model.
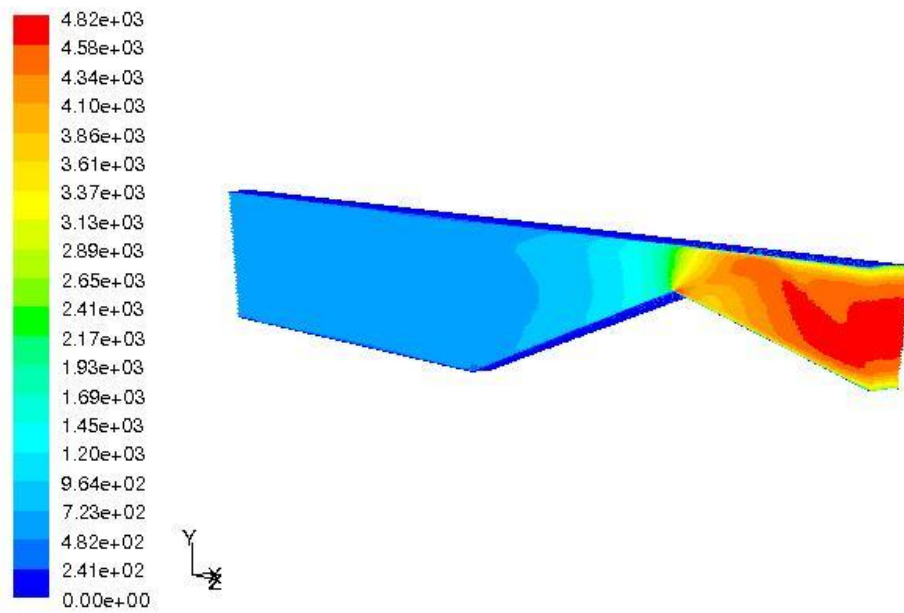
Figure A.8: Velocity Variation for Gas Along Length of the Model.

Contour Plots For The Fluid-Thermal Analysis After The Eighth Firing
Cycle
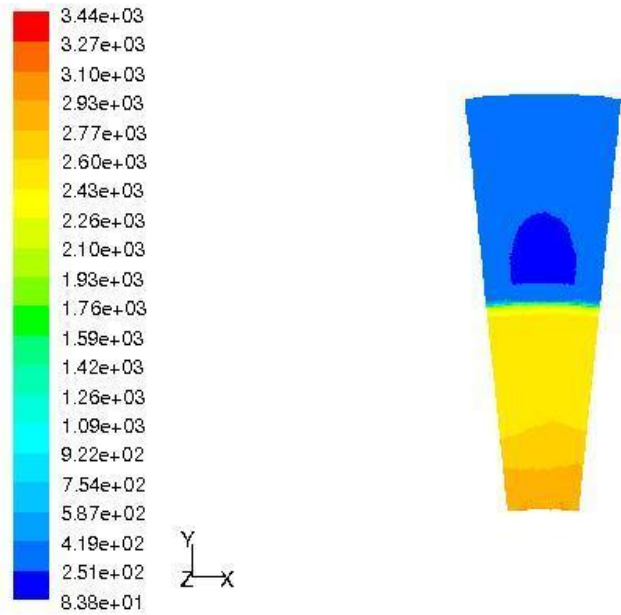
Figure B.1: Cross Sectional Temperature Contours for All Zones in the Model at the Outlet.
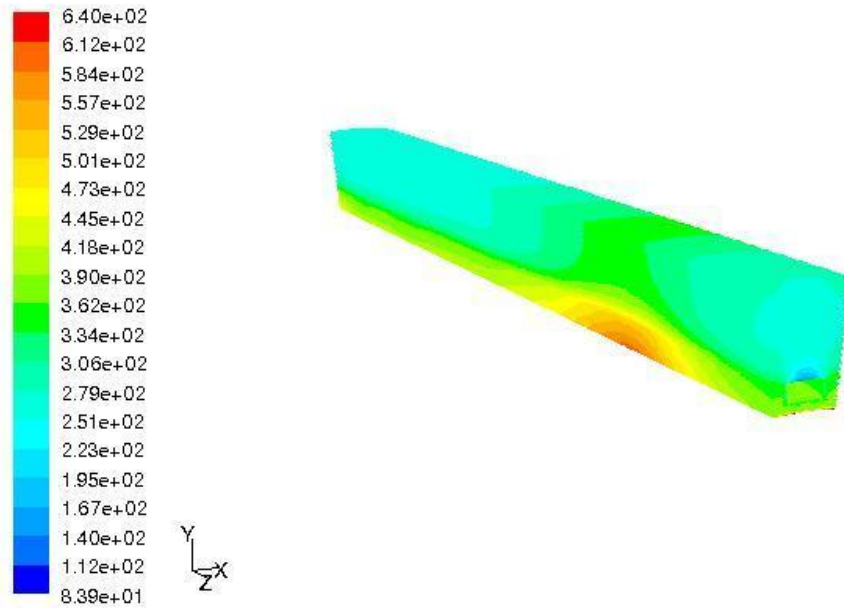
Figure B.2: Temperature Contour in the Solid Zone.
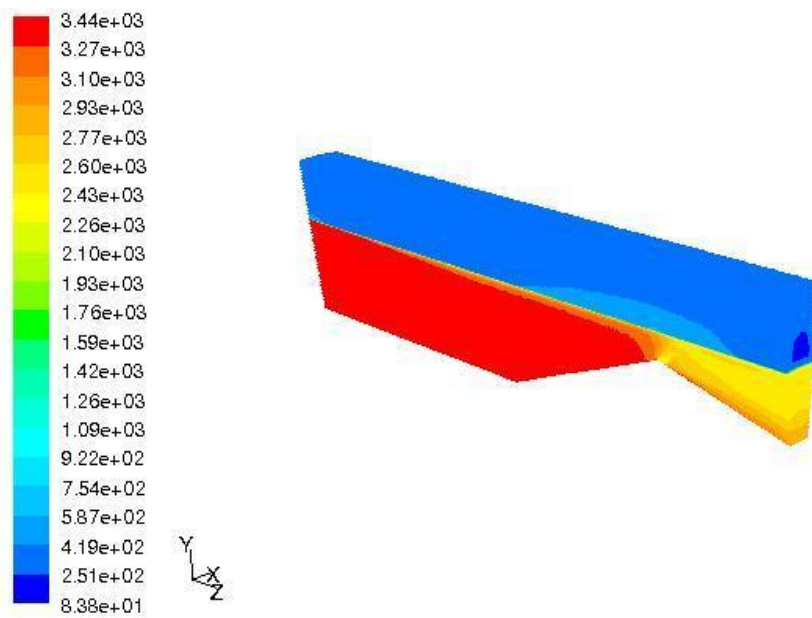
Figure B.3: Temperature Contours for All Fluid and Solid Zones in the Model.
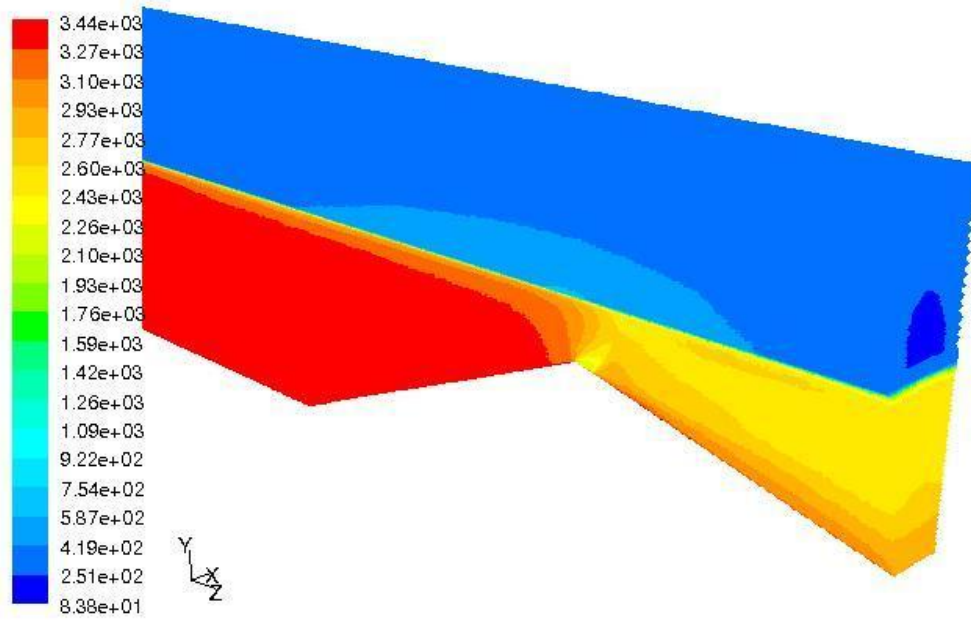
Figure B.4: Temperature Contours Magnified at the Throat Region.
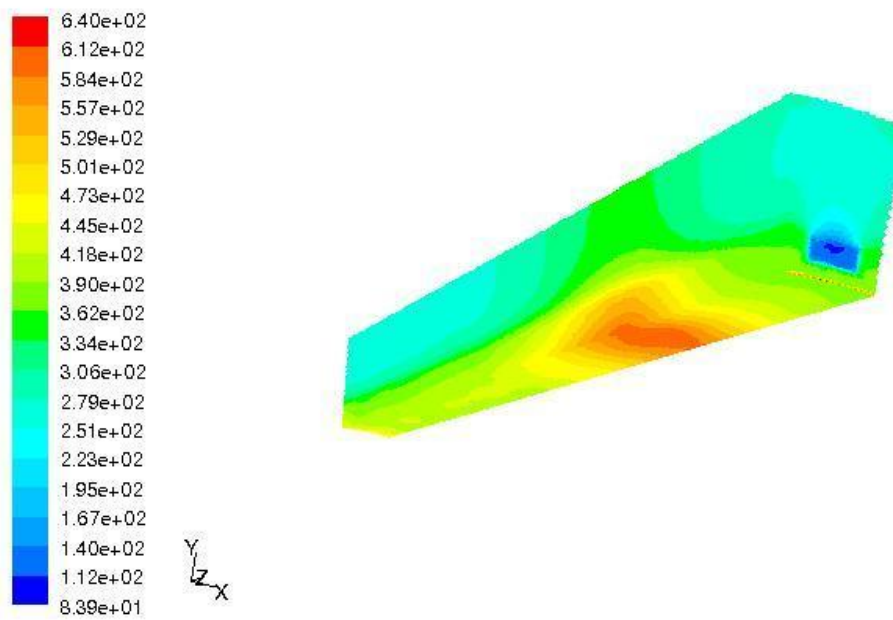
Figure B.5: Temperature Variation Inclusive of the Water Region.
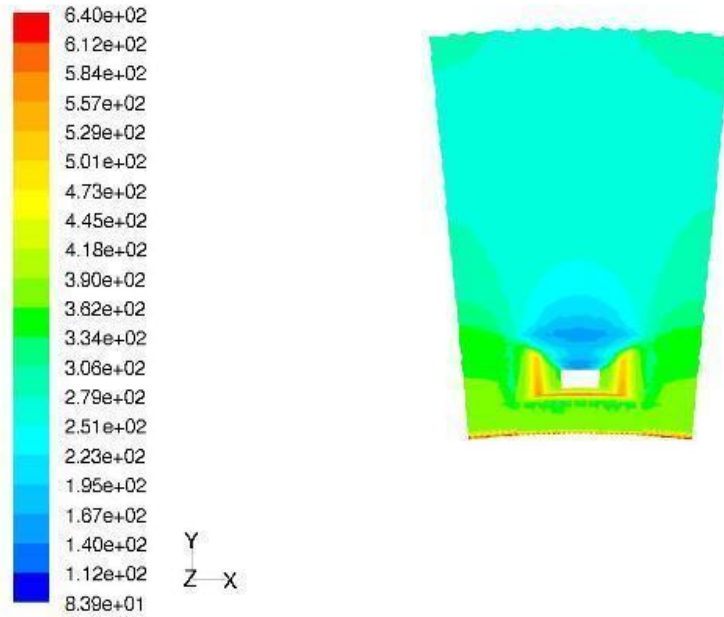
Figure B.6: Cross Sectional View of Temperature Variation at the Outlet.
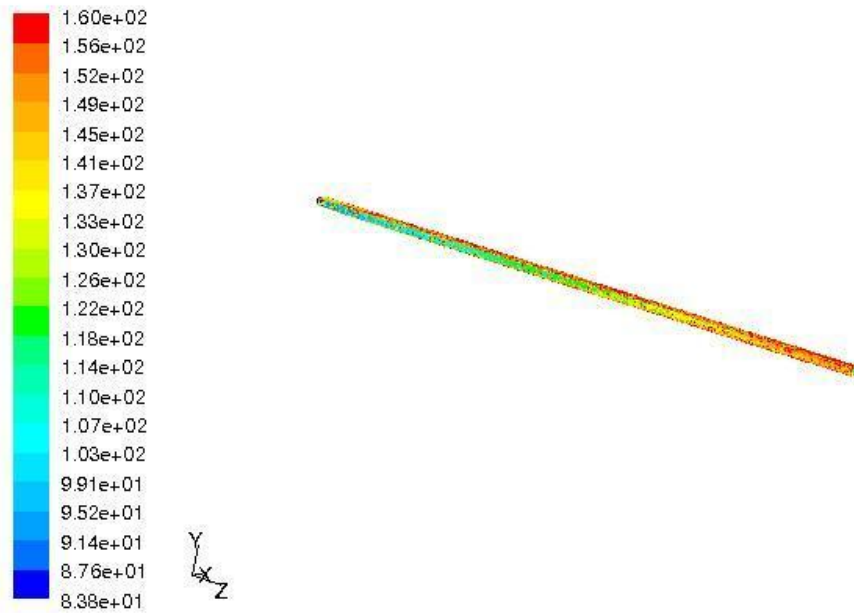
Figure B.7: Temperature Variation For Water Along Length of the Model.
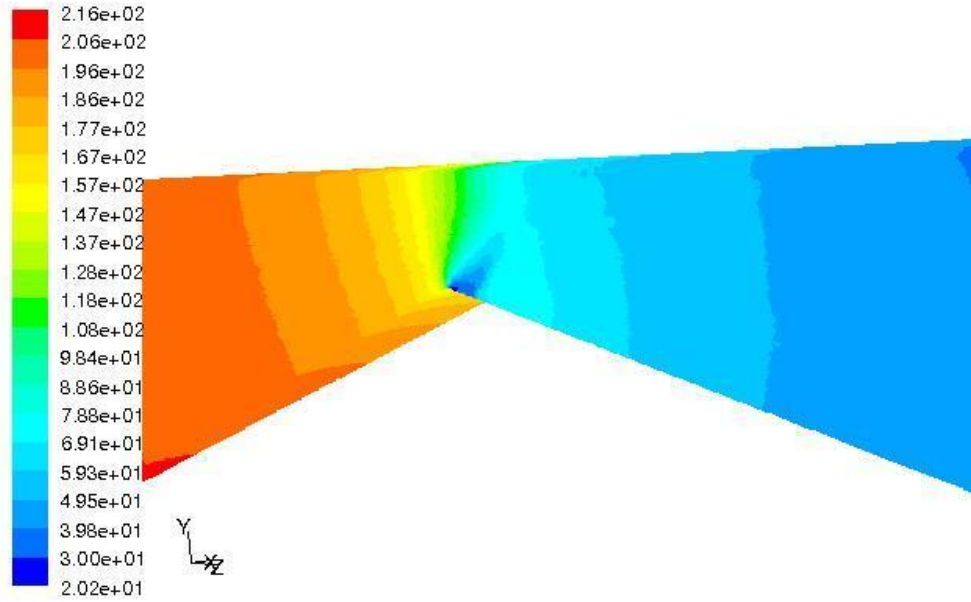
Figure B.8: Pressure Contours Magnified at the Throat Region.
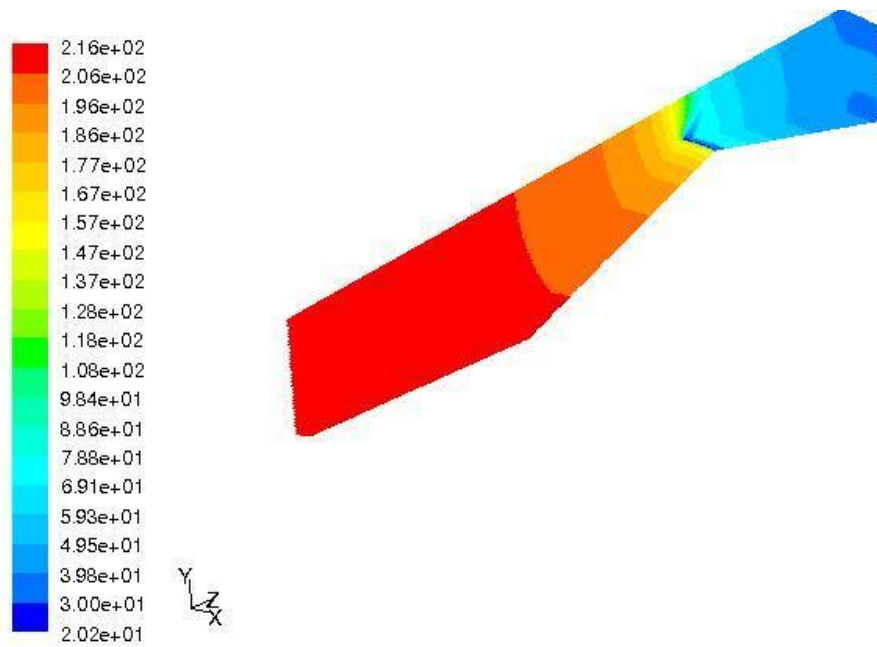
Figure B.9: Fluid Pressure Variation for the Gas Region Along Length of the Model.
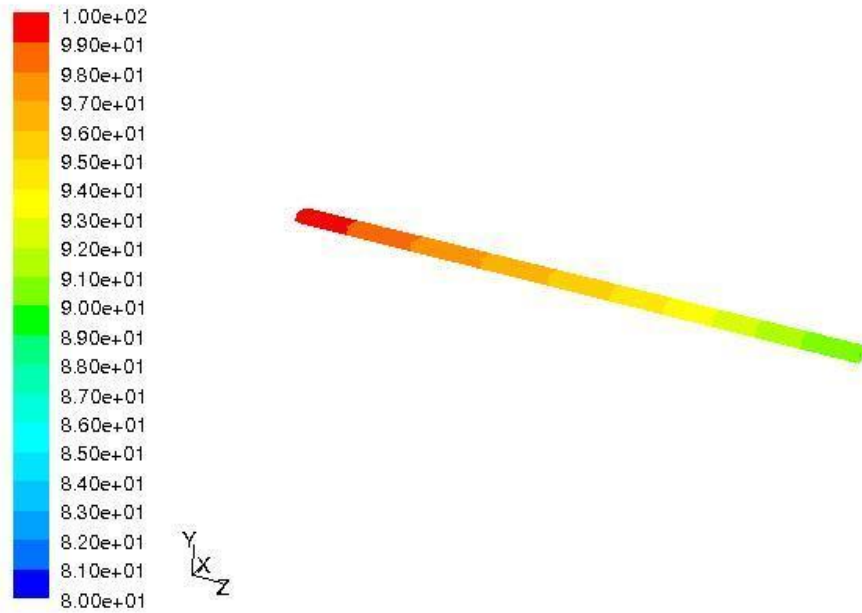
Figure B.10: Fluid Pressure Variation for the Water Region Along Length of the Model.
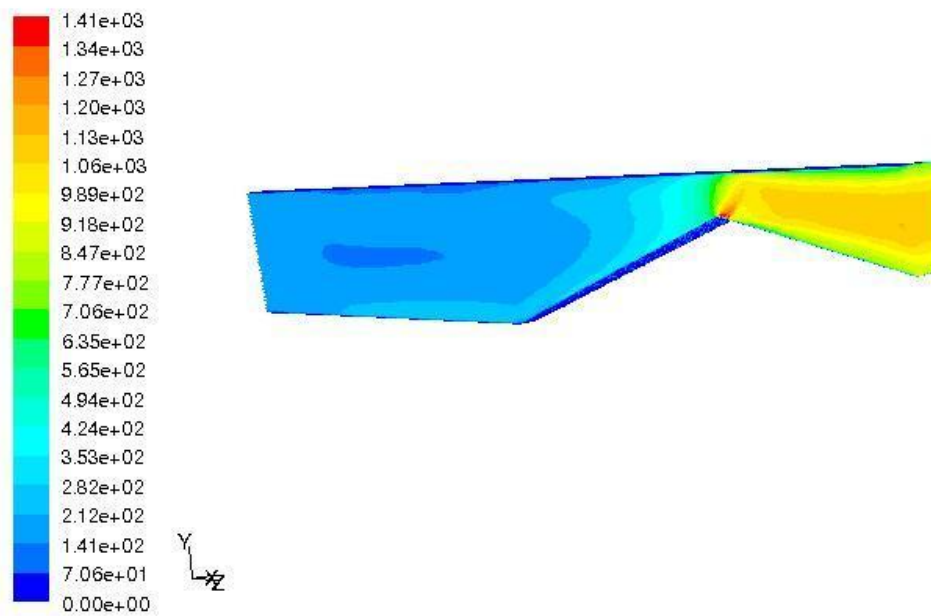
Figure B.11: Fluid Velocity Variation for the Gas Region Along Length of the Model.

65
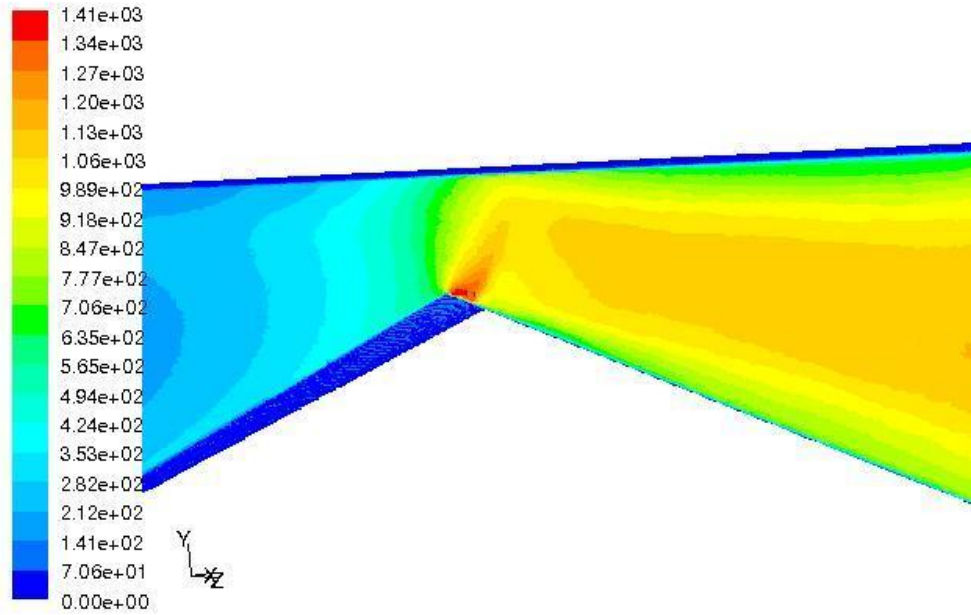
Figure B.12: Velocity Contours Magnified at the Throat Region.
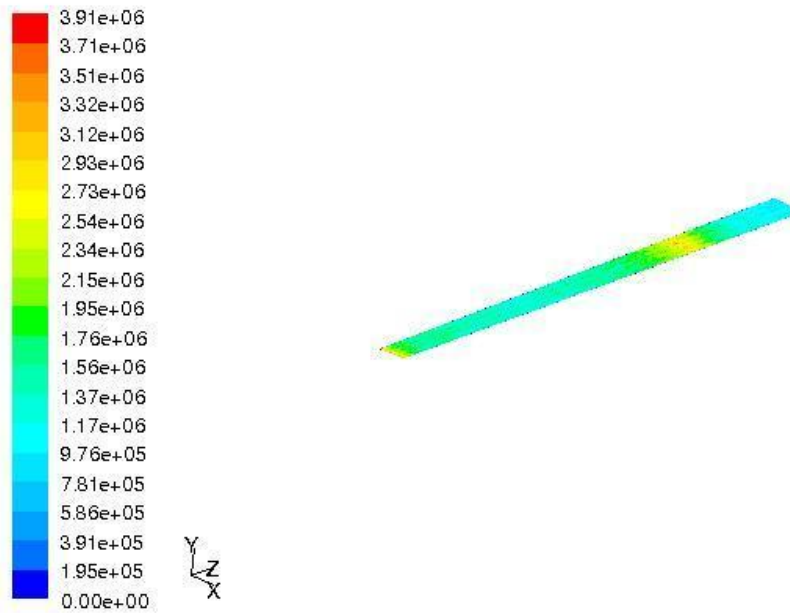
Figure B.13: Heat Flux Variation at Gas Side Wall Along Length of the Model.

Figure C.1: Total Strain - X Component
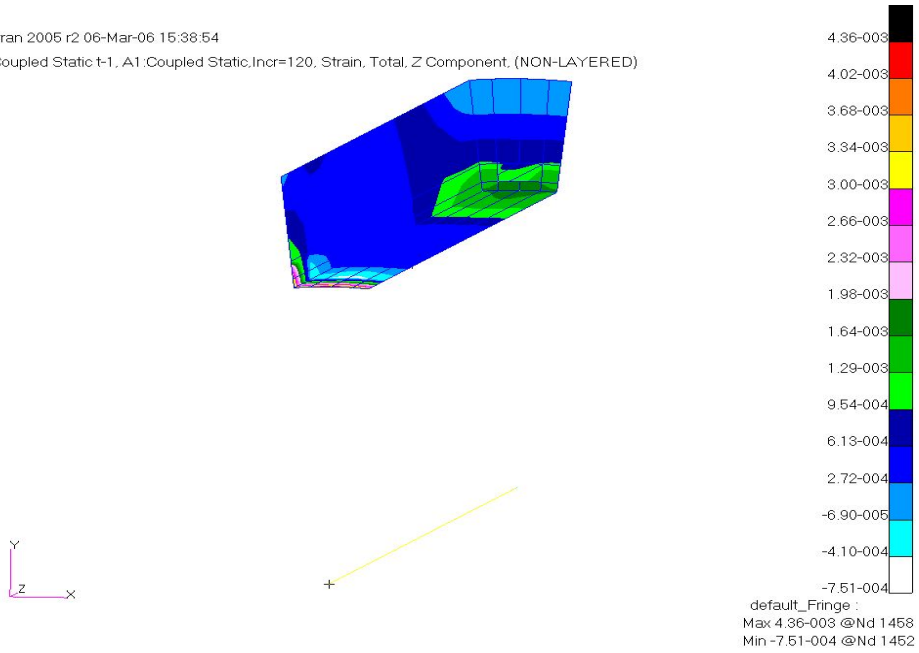
Figure C.2: Total Strain - Z Component
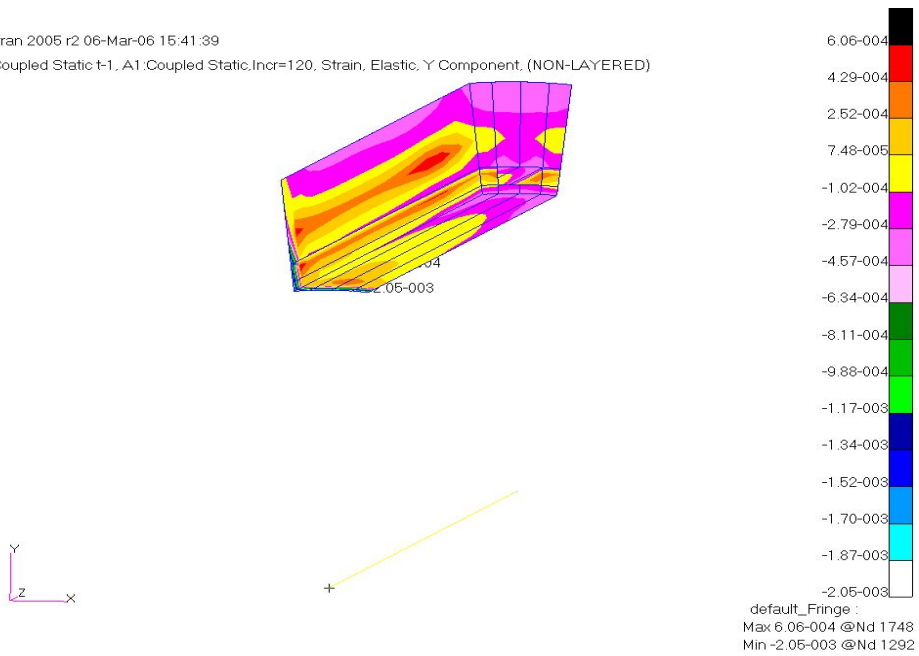
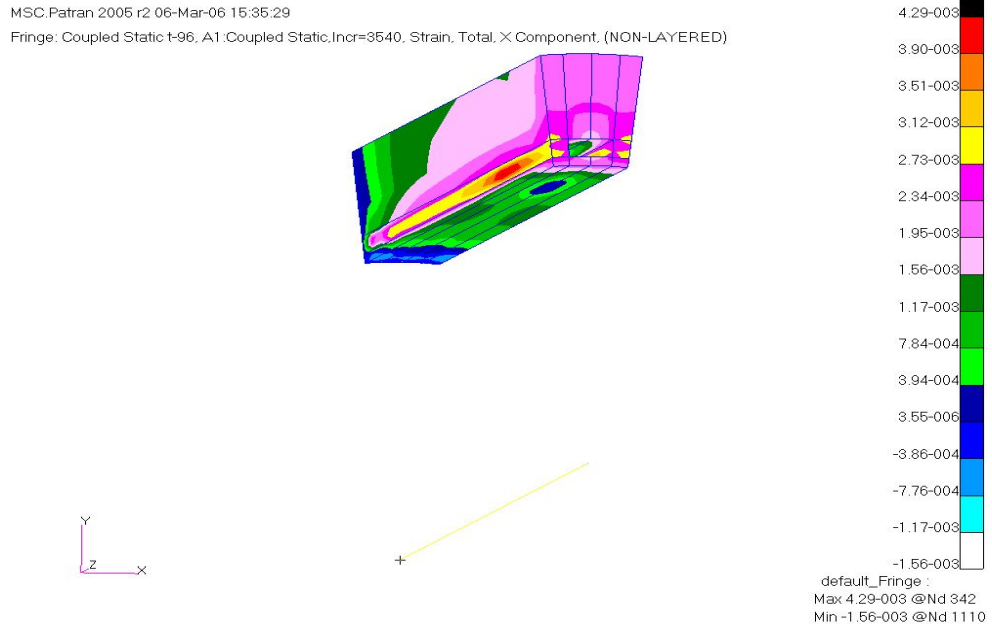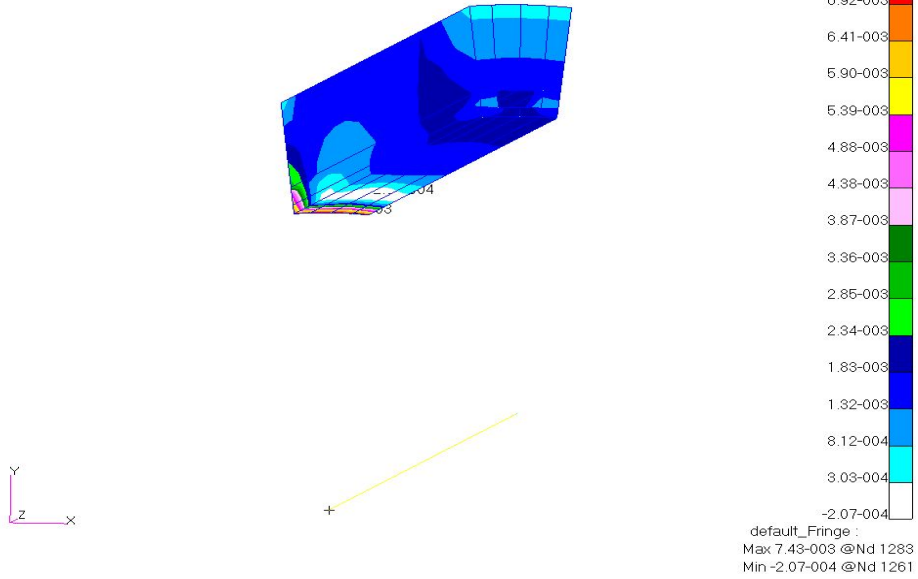Figure C.3: Elastic Strain - Y Component

Figure C.4: Plastic Strain - Y Component
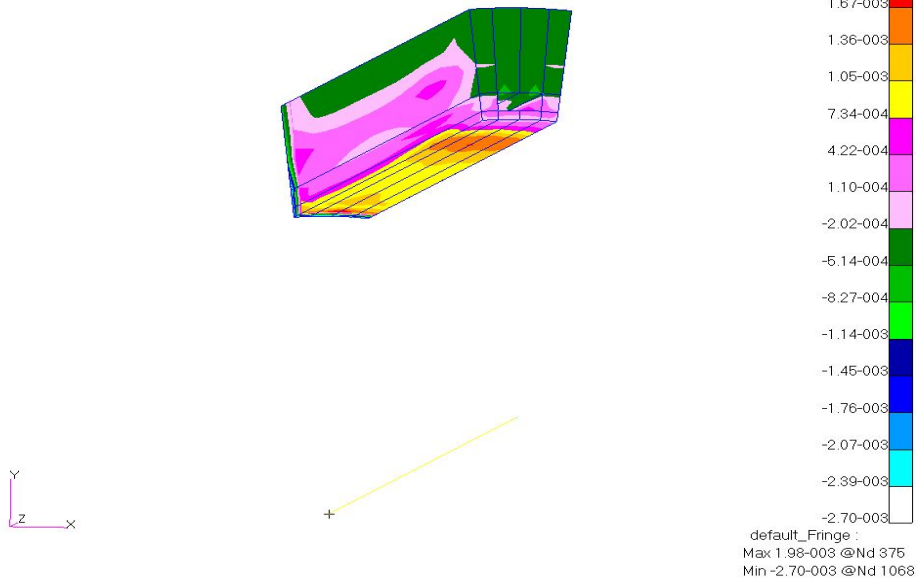

Figure C.5: Thermal Strain - Y Component

MSC.Patran 2005 r2 06-Mar-06 15:27:40
Fringe: Coupled Static t-1, A1:Coupled Static,Incr=120, Displacement, Translation, Magnitude, (NON-LAYERED)

3.14-003
2.93-003
2.72-003
2.51-003
2.30-003
2.10-003
1.89-003
1.68-003
1.47-003
1.26-003
1.05-003
8.38-004
6.29-004
4.19-004
2.10-004
1.68-016

default_Fringe :
Max 3.14-003 @Nd 48
Min 1.68-016 @Nd 1663
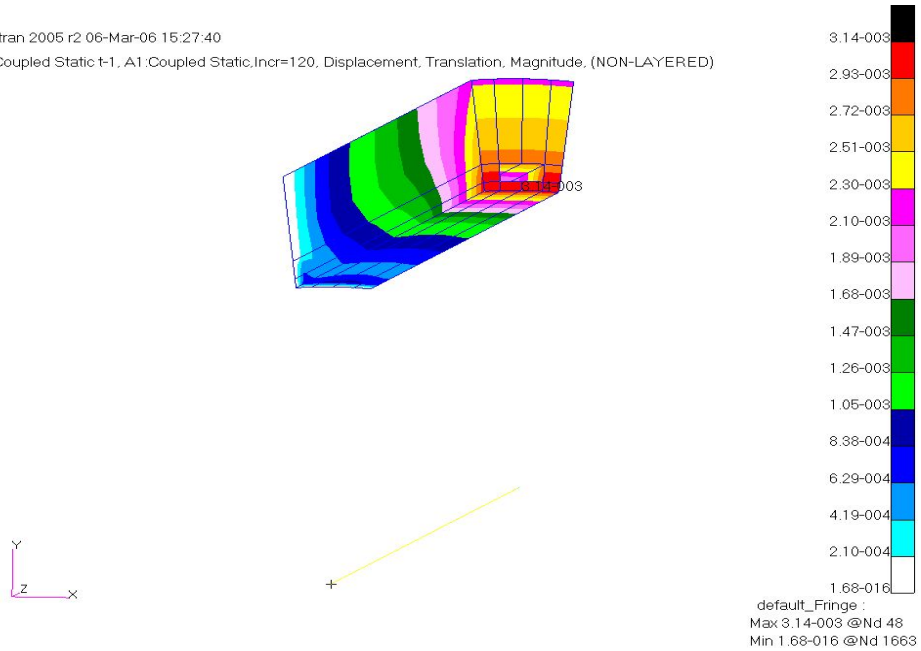
Figure C.6: Displacement Contour - Magnitude

MSC.Patran 2005 r2 06-Mar-06 15:31:28
Fringe: Coupled Static t-1, A1:Coupled Static,Incr=120, Displacement, Translation, X Component, (NON-LAYERED)

2.08-004
1.80-004
1.52-004
1.24-004
9.62-005
6.82-005
4.01-005
1.21-005
-1.59-005
-4.40-005
-7.20-005
-1.00-004
-1.28-004
-1.56-004
-1.84-004
-2.12-004

default_Fringe :
Max 2.08-004 @Nd 357
Min -2.12-004 @Nd 444
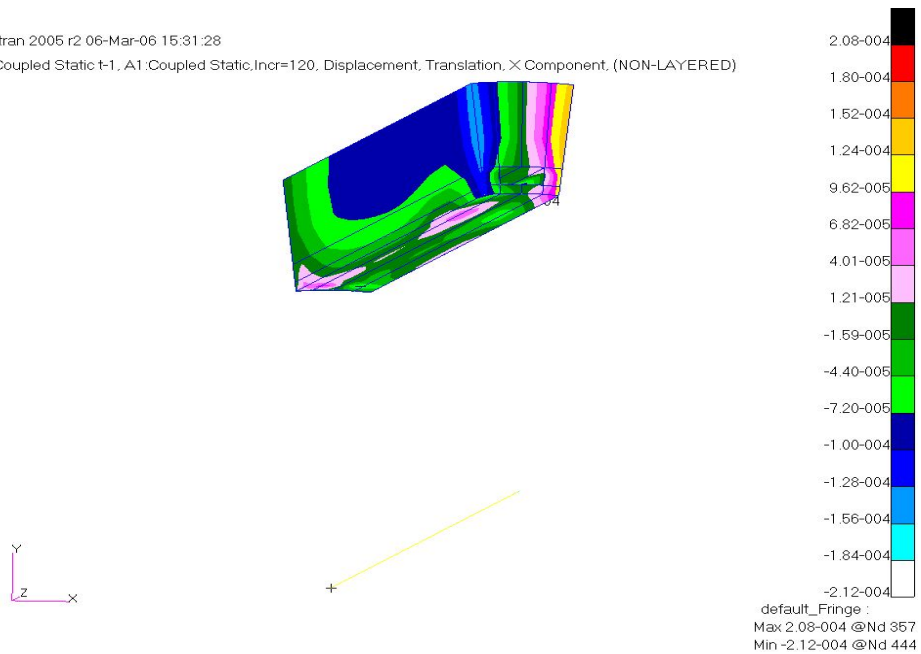
Figure C.7: Displacement Contour - X Component
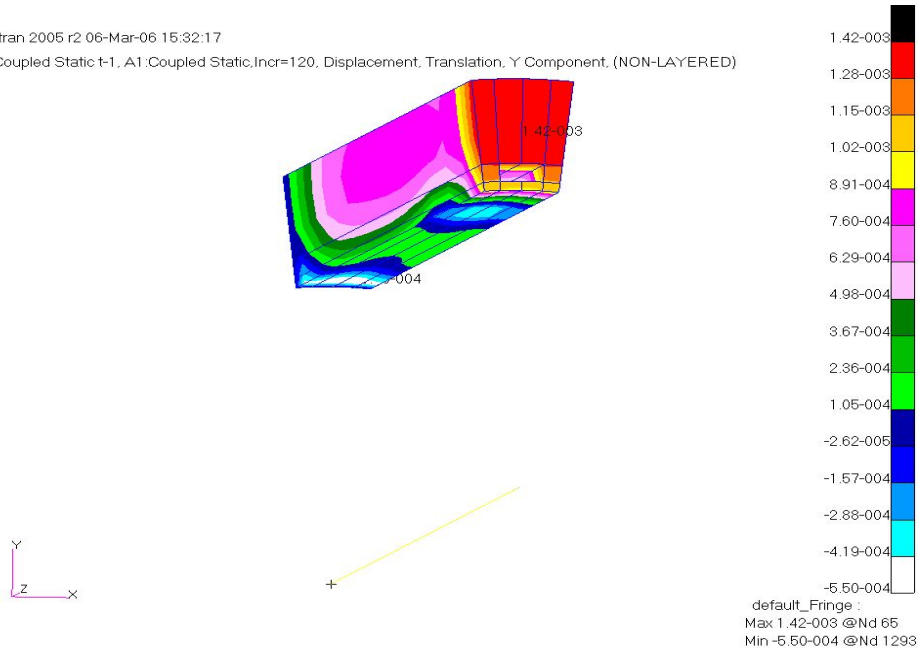
Figure C.8: Displacement Contour - Y Component
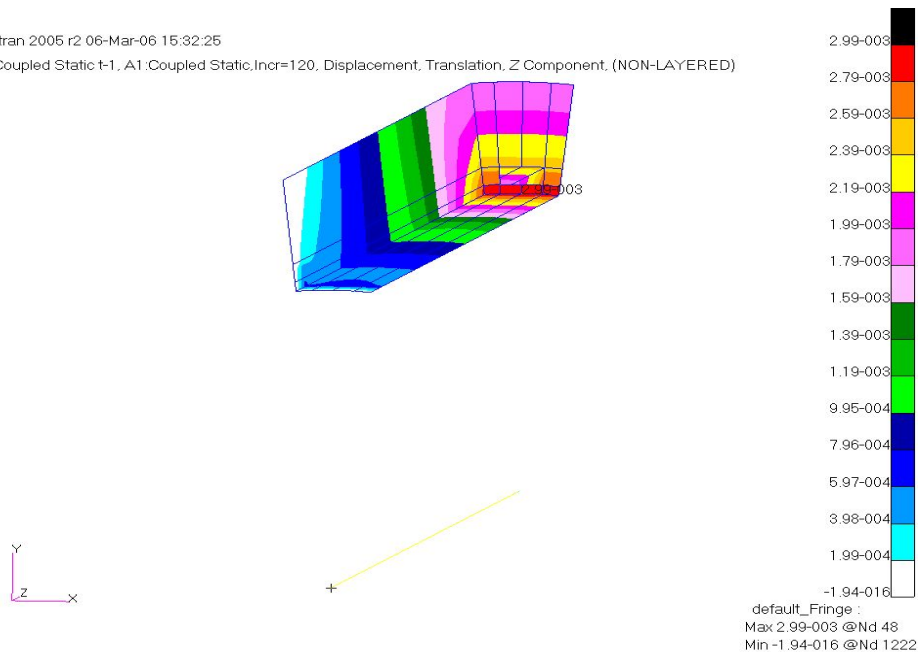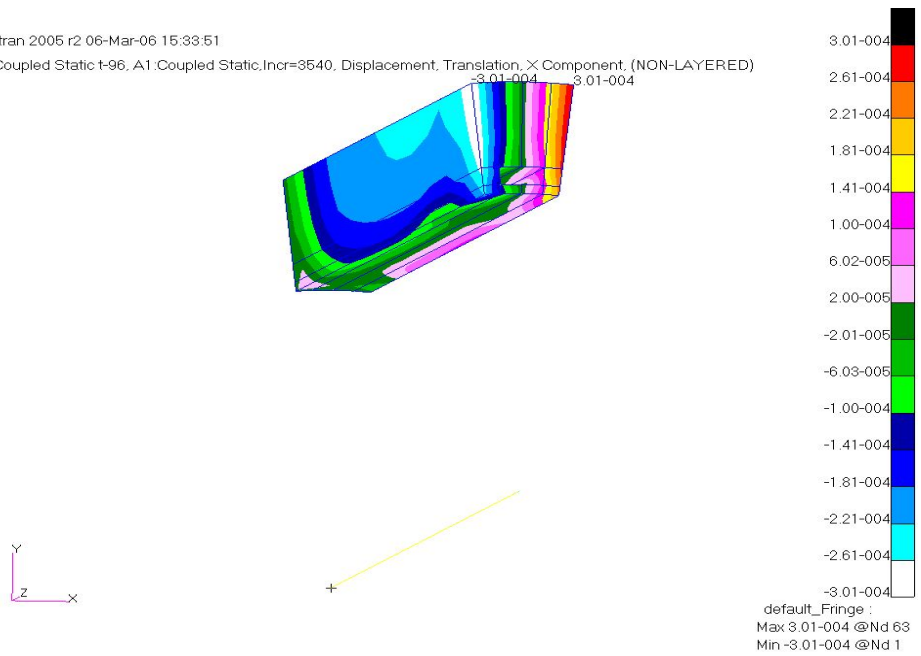

Figure C.9: Displacement Contour - Z Component

MSC.Patran 2005 r2 06-Mar-06 15:54:00

Fringe: Coupled Static t-1, A1:Coupled Static,Incr=120, Stress, Global System, von Mises, At Layer 1

4.84+004
4.53+004
4.21+004
3.90+004
3.58+004
3.27+004
2.95+004
2.64+004
2.32+004
2.01+004
1.69+004
1.38+004
1.06+004
7.46+003
4.31+003
1.16+003

default_Fringe :
Max 4.84+004 @Nd 1702
Min 1.16+003 @Nd 948

Figure C.10: Stress Contour

Contour Plots For The Thermo-Structural Analysis After the Twentieth Firing Cycle

MSC.Patran 2005 r2 06-Mar-06 15:35:29

Fringe: Coupled Static t-96, A1:Coupled Static,Incr=3540, Strain, Total, X Component, (NON-LAYERED)

4.29-003
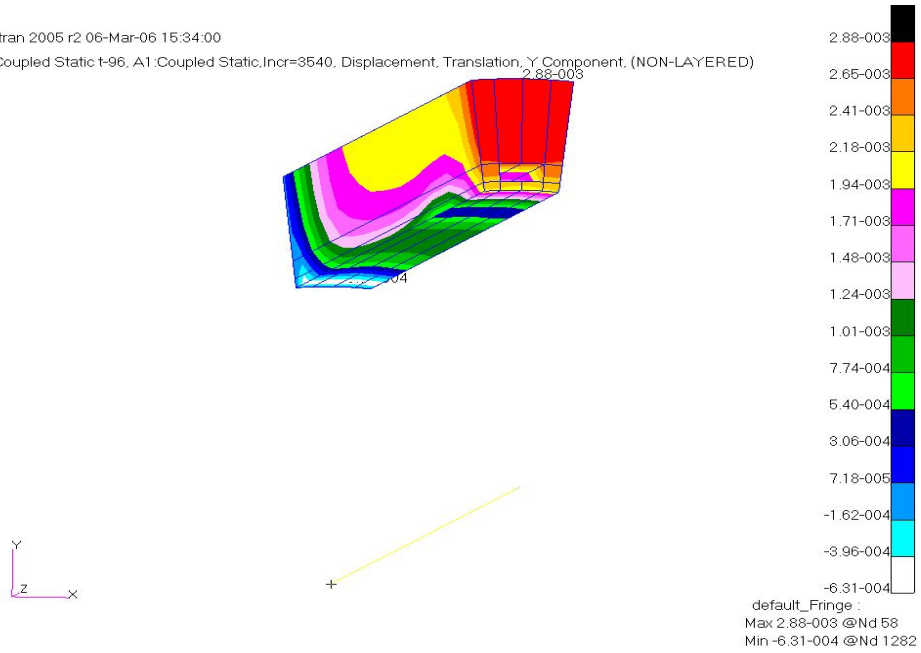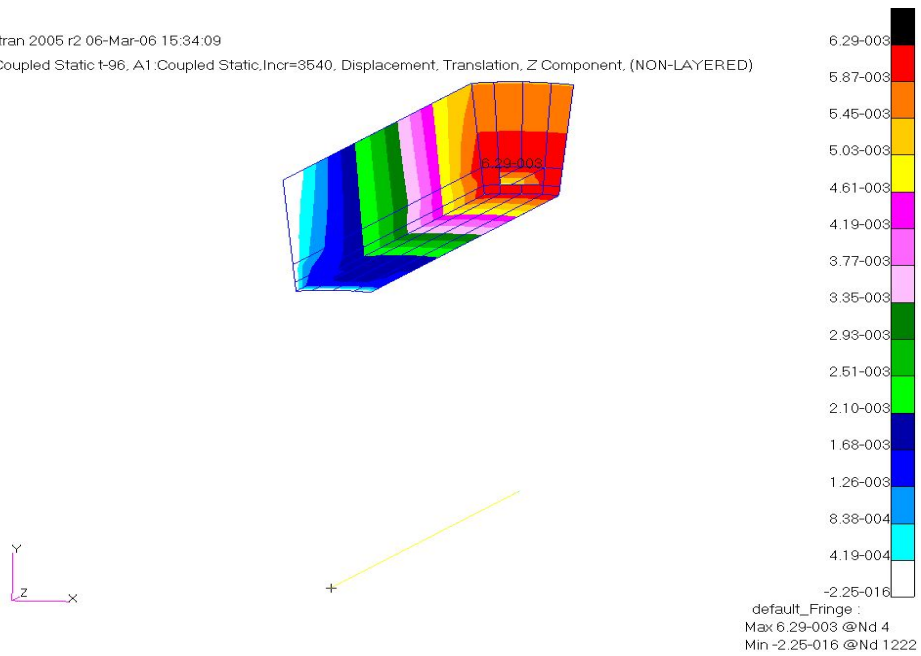3.90-003
3.51-003
3.12-003
2.73-003
2.34-003
1.95-003
1.56-003
1.17-003
7.84-004
3.94-004
3.55-006
-3.86-004
-7.76-004
-1.17-003
-1.56-003

default_Fringe :
Max 4.29-003 @Nd 342
Min -1.56-003 @Nd 1110

Figure D.1: Total Strain - X Component

Figure D.2: Total Strain - Z Component

Figure D.3: Elastic Strain - Y Component
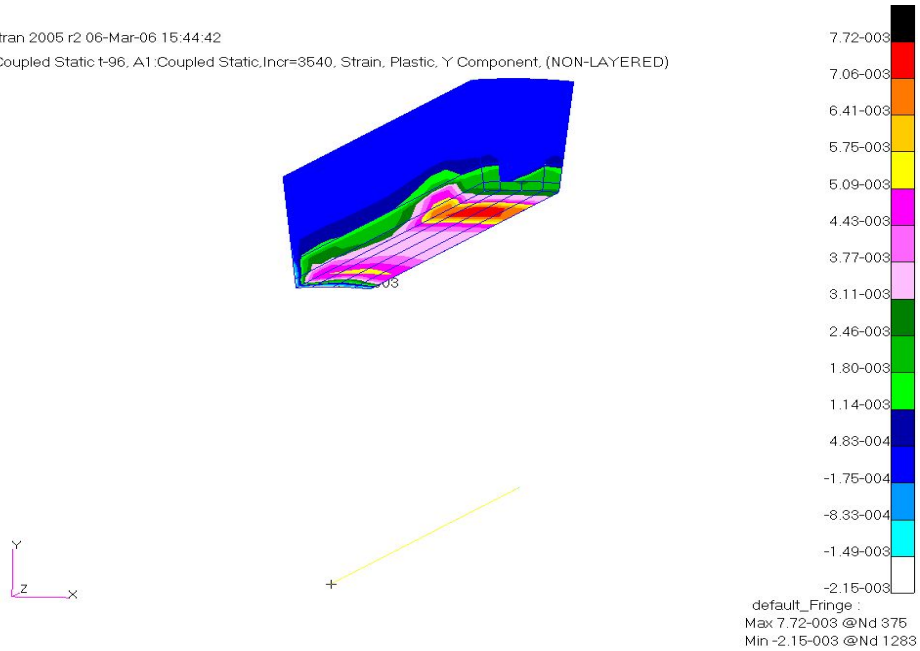
Figure D.4: Plastic Strain - Y Component
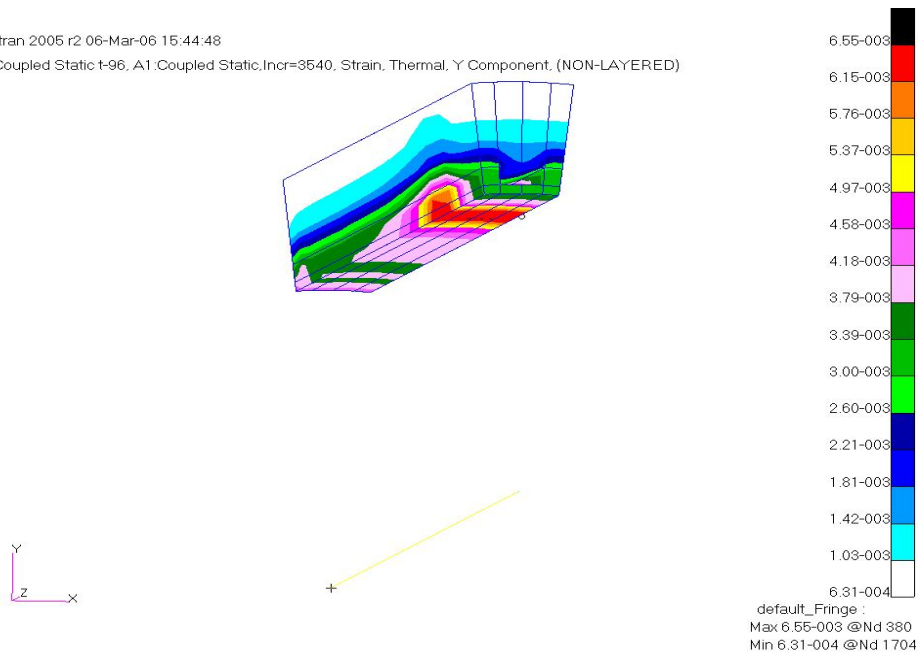
Figure D.5: Thermal Strain - Y Component

Figure D.6: Displacement Contour - Magnitude

Figure D.7: Displacement Contour - X Component

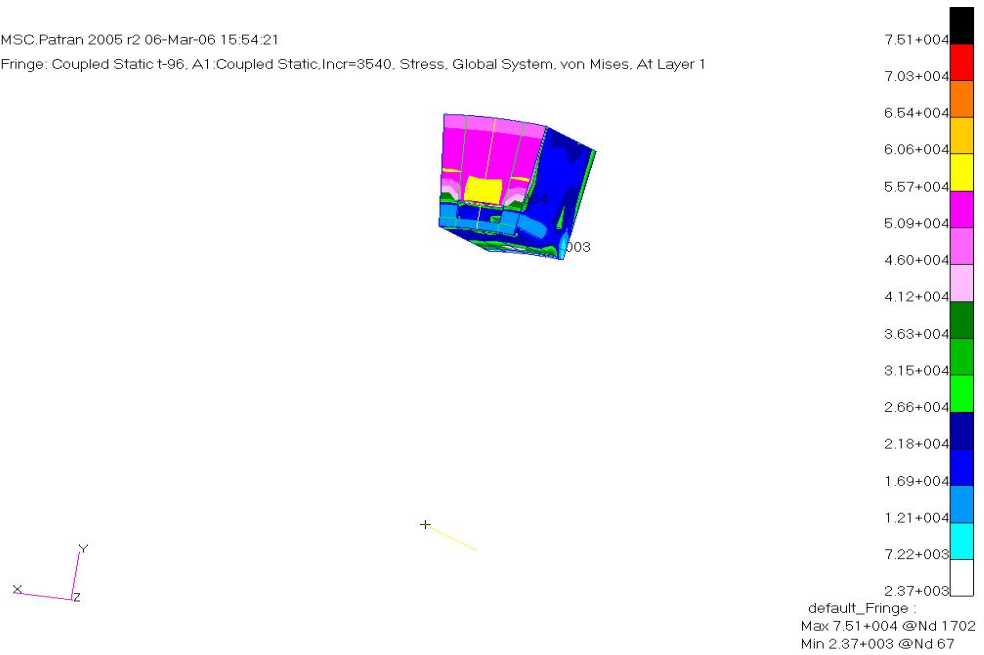Figure D.8: Displacement Contour - Y Component

Figure D.9: Displacement Contour - Z Component

Figure D.10: Stress Contour